

Strangeness Production at low Q^2 in Deep-Inelastic ep Scattering at HERA

H1 Collaboration

Abstract

The production of neutral strange hadrons is investigated using deep-inelastic scattering events measured with the H1 detector at HERA. The measurements are made in the phase space defined by the negative four-momentum transfer squared of the photon $2 < Q^2 < 100 \text{ GeV}^2$ and the inelasticity $0.1 < y < 0.6$. The K_s^0 and $\Lambda(\bar{\Lambda})$ production cross sections and their ratios are determined. K_s^0 production is compared to the production of charged particles in the same region of phase space. The $\Lambda - \bar{\Lambda}$ asymmetry is also measured and found to be consistent with zero. Predictions of leading order Monte Carlo programs are compared to the data.

Accepted by *Eur. Phys. J. C*

F.D. Aaron^{5,49}, C. Alexa⁵, V. Andreev²⁵, B. Antunovic¹¹, S. Aplin¹¹, A. Asmone³³,
 A. Astvatsatourov⁴, A. Bacchetta¹¹, S. Backovic³⁰, A. Baghdasaryan³⁸, E. Barrelet²⁹,
 W. Bartel¹¹, M. Beckingham¹¹, K. Begzsuren³⁵, O. Behnke¹⁴, A. Belousov²⁵, N. Berger⁴⁰,
 J.C. Bizot²⁷, M.-O. Boenig⁸, V. Boudry²⁸, I. Bozovic-Jelisavcic², J. Bracinik³, G. Brandt¹¹,
 M. Brinkmann¹¹, V. Brisson²⁷, D. Bruncko¹⁶, A. Bunyatyan^{13,38}, G. Buschhorn²⁶,
 L. Bystritskaya²⁴, A.J. Campbell¹¹, K.B. Cantun Avila²², F. Cassol-Brunner²¹, K. Cerny³²,
 V. Cerny^{16,47}, V. Chekelian²⁶, A. Cholewa¹¹, J.G. Contreras²², J.A. Coughlan⁶, G. Cozzika¹⁰,
 J. Cvach³¹, J.B. Dainton¹⁸, K. Daum^{37,43}, M. Deák¹¹, Y. de Boer¹¹, B. Delcourt²⁷,
 M. Del Degan⁴⁰, J. Delvax⁴, A. De Roeck^{11,45}, E.A. De Wolf⁴, C. Diaconu²¹, V. Dodonov¹³,
 A. Dossanov²⁶, A. Dubak^{30,46}, G. Eckerlin¹¹, V. Efremenko²⁴, S. Egli³⁶, R. Eichler⁴⁰,
 A. Eliseev²⁵, E. Elsen¹¹, S. Essenov²⁴, A. Falkiewicz⁷, P.J.W. Faulkner³, L. Favart⁴,
 A. Fedotov²⁴, R. Felst¹¹, J. Feltesse^{10,48}, J. Ferencei¹⁶, M. Fleischer¹¹, A. Fomenko²⁵,
 E. Gabathuler¹⁸, J. Gayler¹¹, S. Ghazaryan³⁸, A. Glazov¹¹, I. Glushkov³⁹, L. Goerlich⁷,
 M. Goettlich¹², N. Gogitidze²⁵, M. Gouzevitch²⁸, C. Grab⁴⁰, T. Greenshaw¹⁸, B.R. Grell¹¹,
 G. Grindhammer²⁶, S. Habib^{12,50}, D. Haidt¹¹, M. Hansson²⁰, C. Helebrant¹¹,
 R.C.W. Henderson¹⁷, E. Hennekemper¹⁵, H. Henschel³⁹, G. Herrera²³, M. Hildebrandt³⁶,
 K.H. Hiller³⁹, D. Hoffmann²¹, R. Horisberger³⁶, A. Hovhannisyan³⁸, T. Hreus^{4,44},
 M. Jacquet²⁷, M.E. Janssen¹¹, X. Janssen⁴, V. Jemanov¹², L. Jönsson²⁰, A.W. Jung¹⁵,
 H. Jung¹¹, M. Kapichine⁹, J. Katzy¹¹, I.R. Kenyon³, C. Kiesling²⁶, M. Klein¹⁸, C. Kleinwort¹¹,
 T. Klimkovich¹¹, T. Kluge¹⁸, A. Knutsson¹¹, R. Kogler²⁶, V. Korbel¹¹, P. Kostka³⁹,
 M. Kraemer¹¹, K. Krastev¹¹, J. Kretzschmar¹⁸, A. Kropivnitskaya²⁴, K. Krüger¹⁵, K. Kutak¹¹,
 M.P.J. Landon¹⁹, W. Lange³⁹, G. Laštovička-Medin³⁰, P. Laycock¹⁸, A. Lebedev²⁵,
 G. Leibenguth⁴⁰, V. Lendermann¹⁵, S. Levonian¹¹, G. Li²⁷, K. Lipka¹², A. Liptaj²⁶, B. List¹²,
 J. List¹¹, N. Loktionova²⁵, R. Lopez-Fernandez²³, V. Lubimov²⁴, A.-I. Lucaci-Timoce¹¹,
 L. Lytkin¹³, A. Makankine⁹, E. Malinovski²⁵, P. Marage⁴, Ll. Marti¹¹, H.-U. Martyn¹,
 S.J. Maxfield¹⁸, A. Mehta¹⁸, K. Meier¹⁵, A.B. Meyer¹¹, H. Meyer¹¹, H. Meyer³⁷, J. Meyer¹¹,
 V. Michels¹¹, S. Mikocki⁷, I. Milcewicz-Mika⁷, F. Moreau²⁸, A. Morozov⁹, J.V. Morris⁶,
 M.U. Mozer⁴, M. Mudrinic², K. Müller⁴¹, P. Murín^{16,44}, K. Nankov³⁴, B. Naroska^{12,†},
 Th. Naumann³⁹, P.R. Newman³, C. Niebuhr¹¹, A. Nikiforov¹¹, G. Nowak⁷, K. Nowak⁴¹,
 M. Nozicka¹¹, B. Olivier²⁶, J.E. Olsson¹¹, S. Osman²⁰, D. Ozerov²⁴, V. Palichik⁹,
 I. Panagoulas^{1,11,42}, M. Pandurovic², Th. Papadopoulou^{1,11,42}, C. Pascaud²⁷, G.D. Patel¹⁸,
 O. Pejchal³², H. Peng¹¹, E. Perez^{10,45}, A. Petrukhin²⁴, I. Picuric³⁰, S. Piec³⁹, D. Pitzl¹¹,
 R. Plačakytė¹¹, R. Polifka³², B. Povh¹³, T. Preda⁵, V. Radescu¹¹, A.J. Rahmat¹⁸, N. Raicevic³⁰,
 A. Rapiareza²⁶, T. Ravdandorj³⁵, P. Reimer³¹, E. Rizvi¹⁹, P. Robmann⁴¹, B. Roland⁴,
 R. Roosen⁴, A. Rostovtsev²⁴, M. Rotaru⁵, J.E. Ruiz Tabasco²², Z. Rurikova¹¹, S. Rusakov²⁵,
 D. Salek³², F. Salvaire¹¹, D.P.C. Sankey⁶, M. Sauter⁴⁰, E. Sauvan²¹, S. Schmidt¹¹,
 S. Schmitt¹¹, C. Schmitz⁴¹, L. Schoeffel¹⁰, A. Schöning^{11,41}, H.-C. Schultz-Coulon¹⁵,
 F. Sefkow¹¹, R.N. Shaw-West³, I. Sheviakov²⁵, L.N. Shtarkov²⁵, S. Shushkevich²⁶, T. Sloan¹⁷,
 I. Smiljanic², P. Smirnov²⁵, Y. Soloviev²⁵, P. Sopicki⁷, D. South⁸, V. Spaskov⁹, A. Specka²⁸,
 Z. Staykova¹¹, M. Steder¹¹, B. Stella³³, U. Straumann⁴¹, D. Sunar⁴, T. Sykora⁴,
 V. Tchoulakov⁹, G. Thompson¹⁹, P.D. Thompson³, T. Toll¹¹, F. Tomasz¹⁶, T.H. Tran²⁷,
 D. Traynor¹⁹, T.N. Trinh²¹, P. Truöl⁴¹, I. Tsakov³⁴, B. Tsepeldorj^{35,51}, I. Tsurin³⁹, J. Turnau⁷,
 E. Tzamariudaki²⁶, K. Urban¹⁵, A. Valkárová³², C. Vallée²¹, P. Van Mechelen⁴, A. Vargas
 Trevino¹¹, Y. Vazdik²⁵, S. Vinokurova¹¹, V. Volchinski³⁸, D. Wegener⁸, M. Wessels¹¹,
 Ch. Wissing¹¹, E. Wunsch¹¹, V. Yeganov³⁸, J. Žáček³², J. Zálešák³¹, Z. Zhang²⁷,
 A. Zhelezov²⁴, A. Zhokin²⁴, Y.C. Zhu¹¹, T. Zimmermann⁴⁰, H. Zohrabyan³⁸, and F. Zomer²⁷

- ¹ *I. Physikalisches Institut der RWTH, Aachen, Germany^a*
- ² *Vinca Institute of Nuclear Sciences, Belgrade, Serbia*
- ³ *School of Physics and Astronomy, University of Birmingham, Birmingham, UK^b*
- ⁴ *Inter-University Institute for High Energies ULB-VUB, Brussels; Universiteit Antwerpen, Antwerpen; Belgium^c*
- ⁵ *National Institute for Physics and Nuclear Engineering (NIPNE) , Bucharest, Romania*
- ⁶ *Rutherford Appleton Laboratory, Chilton, Didcot, UK^b*
- ⁷ *Institute for Nuclear Physics, Cracow, Poland^d*
- ⁸ *Institut für Physik, TU Dortmund, Dortmund, Germany^a*
- ⁹ *Joint Institute for Nuclear Research, Dubna, Russia*
- ¹⁰ *CEA, DSM/Irfu, CE-Saclay, Gif-sur-Yvette, France*
- ¹¹ *DESY, Hamburg, Germany*
- ¹² *Institut für Experimentalphysik, Universität Hamburg, Hamburg, Germany^a*
- ¹³ *Max-Planck-Institut für Kernphysik, Heidelberg, Germany*
- ¹⁴ *Physikalisches Institut, Universität Heidelberg, Heidelberg, Germany^a*
- ¹⁵ *Kirchhoff-Institut für Physik, Universität Heidelberg, Heidelberg, Germany^a*
- ¹⁶ *Institute of Experimental Physics, Slovak Academy of Sciences, Košice, Slovak Republic^f*
- ¹⁷ *Department of Physics, University of Lancaster, Lancaster, UK^b*
- ¹⁸ *Department of Physics, University of Liverpool, Liverpool, UK^b*
- ¹⁹ *Queen Mary and Westfield College, London, UK^b*
- ²⁰ *Physics Department, University of Lund, Lund, Sweden^g*
- ²¹ *CPPM, CNRS/IN2P3 - Univ. Mediterranee, Marseille - France*
- ²² *Departamento de Fisica Aplicada, CINVESTAV, Mérida, Yucatán, México^j*
- ²³ *Departamento de Fisica, CINVESTAV, México^j*
- ²⁴ *Institute for Theoretical and Experimental Physics, Moscow, Russia*
- ²⁵ *Lebedev Physical Institute, Moscow, Russia^e*
- ²⁶ *Max-Planck-Institut für Physik, München, Germany*
- ²⁷ *LAL, Univ Paris-Sud, CNRS/IN2P3, Orsay, France*
- ²⁸ *LLR, Ecole Polytechnique, IN2P3-CNRS, Palaiseau, France*
- ²⁹ *LPNHE, Universités Paris VI and VII, IN2P3-CNRS, Paris, France*
- ³⁰ *Faculty of Science, University of Montenegro, Podgorica, Montenegro^e*
- ³¹ *Institute of Physics, Academy of Sciences of the Czech Republic, Praha, Czech Republic^h*
- ³² *Faculty of Mathematics and Physics, Charles University, Praha, Czech Republic^h*
- ³³ *Dipartimento di Fisica Università di Roma Tre and INFN Roma 3, Roma, Italy*
- ³⁴ *Institute for Nuclear Research and Nuclear Energy, Sofia, Bulgaria^e*
- ³⁵ *Institute of Physics and Technology of the Mongolian Academy of Sciences , Ulaanbaatar, Mongolia*
- ³⁶ *Paul Scherrer Institut, Villigen, Switzerland*
- ³⁷ *Fachbereich C, Universität Wuppertal, Wuppertal, Germany*
- ³⁸ *Yerevan Physics Institute, Yerevan, Armenia*
- ³⁹ *DESY, Zeuthen, Germany*
- ⁴⁰ *Institut für Teilchenphysik, ETH, Zürich, Switzerlandⁱ*
- ⁴¹ *Physik-Institut der Universität Zürich, Zürich, Switzerlandⁱ*
- ⁴² *Also at Physics Department, National Technical University, Zografou Campus, GR-15773 Athens, Greece*

- ⁴³ Also at Rechenzentrum, Universität Wuppertal, Wuppertal, Germany
⁴⁴ Also at University of P.J. Šafárik, Košice, Slovak Republic
⁴⁵ Also at CERN, Geneva, Switzerland
⁴⁶ Also at Max-Planck-Institut für Physik, München, Germany
⁴⁷ Also at Comenius University, Bratislava, Slovak Republic
⁴⁸ Also at DESY and University Hamburg, Helmholtz Humboldt Research Award
⁴⁹ Also at Faculty of Physics, University of Bucharest, Bucharest, Romania
⁵⁰ Supported by a scholarship of the World Laboratory Björn Wiik Research Project
⁵¹ Also at Ulaanbaatar University, Ulaanbaatar, Mongolia
† Deceased

^a Supported by the Bundesministerium für Bildung und Forschung, FRG, under contract numbers 05 H1 1GUA /1, 05 H1 1PAA /1, 05 H1 1PAB /9, 05 H1 1PEA /6, 05 H1 1VHA /7 and 05 H1 1VHB /5

^b Supported by the UK Science and Technology Facilities Council, and formerly by the UK Particle Physics and Astronomy Research Council

^c Supported by FNRS-FWO-Vlaanderen, IISN-IKW and IWT and by Interuniversity Attraction Poles Programme, Belgian Science Policy

^d Partially Supported by Polish Ministry of Science and Higher Education, grant PBS/DESY/70/2006 and grant N202 2956 33

^e Supported by the Deutsche Forschungsgemeinschaft

^f Supported by VEGA SR grant no. 2/7062/ 27

^g Supported by the Swedish Natural Science Research Council

^h Supported by the Ministry of Education of the Czech Republic under the projects LC527, INGO-1P05LA259 and MSM0021620859

ⁱ Supported by the Swiss National Science Foundation

^j Supported by CONACYT, México, grant 48778-F

^l This project is co-funded by the European Social Fund (75%) and National Resources (25%) - (EPEAEK II) - PYTHAGORAS II

1 Introduction

The production of strange hadrons in high energy particle collisions allows the investigation of strong interactions in the perturbative and non-perturbative regimes. Strange quarks are created in the non-perturbative process of colour string fragmentation, which constitutes the dominant production mechanism of strange hadrons. In deep-inelastic scattering (DIS), strange quarks also originate from the strange sea in the nucleon, boson-gluon fusion and heavy quark decays. Measurements of strangeness production have been used to investigate the suppression of strangeness relative to lighter flavours in fragmentation. The universality of fragmentation in different processes can be studied by comparing differential cross sections of the production of K_s^0 and $\Lambda(\bar{\Lambda})$ hadrons in various regions of phase space. Further information is gained by studying the ratios of production rates of $\Lambda(\bar{\Lambda})$ to K_s^0 and of K_s^0 to charged hadrons (h^\pm) as some model dependencies are expected to cancel.

The baryon production mechanism was studied in e^+e^- annihilation [1, 2, 3, 4, 5], a process without incident baryons. Data involving a baryon in the initial state, like ep collisions at HERA, provide additional information. In particular, data on the $\Lambda - \bar{\Lambda}$ production asymmetry from HERA are of interest as an experimental constraint for theories of baryon number transfer [6]. Fixed target data have shown [7] that the Λ production rate substantially exceeds that of the $\bar{\Lambda}$ in the so-called remnant region because the baryon number of the target is conserved.

This paper presents a measurement of neutral strange particle (K_s^0 and Λ) production in DIS at negative four momentum transfer squared $2 < Q^2 < 100 \text{ GeV}^2$ and at low values of Bjorken x . The study is based on data collected with the H1 detector at HERA at a centre-of-mass energy of 319 GeV in the years 1999 and 2000. This data sample is 40 times larger than that used in the previous H1 publication [8] and covers a wider kinematic range. Measurements of K_s^0 and Λ production in different kinematic ranges have also been reported by the ZEUS collaboration [9]. The differential cross sections of K_s^0 mesons, $\Lambda(\bar{\Lambda})$ baryons and their ratio as well as the ratio of K_s^0 to charged hadrons are presented as a function of various kinematic variables, both in the laboratory frame and in the Breit frame. The results are compared with predictions obtained from leading order Monte Carlo calculations, based on matrix elements, with parton shower simulations. The main feature of the data is a suppression of strange quark production relative to lighter quarks; this is discussed within the context of the framework of the LUND [10] fragmentation model.

2 Phenomenology

2.1 Production of Strange Hadrons

Particles with strangeness can be produced in DIS in the hard sub-process and in the hadronisation of the colour field, as illustrated schematically in figure 1.

Figure 1a) shows strangeness production within the quark parton model (QPM), where a strange quark s from the nucleon sea participates in the hard interaction. Figure 1b) illustrates s production in a boson-gluon fusion (BGF) process, where a gluon emitted from the nucleon

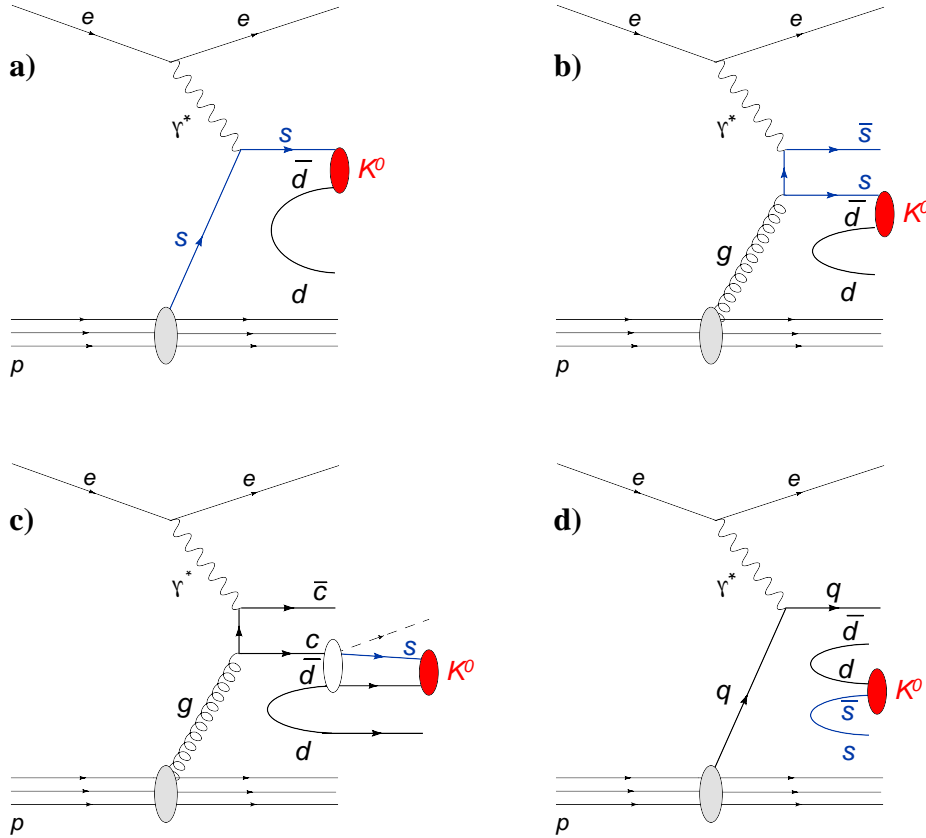


Figure 1: Schematic diagrams of the different processes contributing to strangeness production: a) direct production in the QPM, b) BGF, c) decays of heavy quarks and d) hadronisation.

splits into a $s\bar{s}$ quark pair. Figure 1c) depicts heavy quark (charm c and beauty b) production by boson-gluon fusion (BGF) with subsequent weak decay into $s(\bar{s})$ quarks. This process is suppressed at low Q^2 due to the masses of the heavy quarks. These production mechanisms (figures 1a, b, c) are characterised by a hard scale allowing for a perturbative treatment. The relative rate of the BGF processes depends strongly on the Bjorken scaling variable x due to the strong rise of the gluon density at low x . In the kinematic region studied in this analysis (low x) the BGF contributions are expected to be significant. According to the Monte Carlo predictions described below, roughly 25% of the strange hadrons originate from strange quarks produced in the hard interaction either directly (figures 1a and b) or through heavy quark production in BGF processes (figure 1c). In regions of phase space where the quark masses are not relevant with respect to the process scales (e.g. at very high Q^2) this rate can reach up to 50%.

The largest contribution to strange quark production is due to the colour field fragmentation processes, as illustrated in figure 1d). As these processes occur at large distances they cannot be treated perturbatively and thus phenomenological models, such as the LUND string model [10], are required for their description.

Frames of reference customarily used to study particle production are the laboratory and the Breit frame [11]. In the Breit frame of reference the virtual space-like photon has momentum Q but no energy. The photon direction defines the negative z -axis with the proton moving in the $+z$

direction. The transverse momentum in the Breit frame p_T^{Breit} is computed with respect to this axis. Particles from the proton remnant are almost collinear to the incoming proton direction, therefore the hemisphere defined by $p_z^{Breit} > 0$ is labelled as the target hemisphere. Equally, in the QPM the struck quark only populates the current hemisphere ($p_z^{Breit} < 0$). Higher order processes modify this simple picture as they generate transverse momentum in the final state and may lead to particles from the hard subprocess propagating into the target hemisphere.

In the current hemisphere, the mechanism of particle production should in principle resemble that of collisions without an incident proton like e^+e^- . In analogy with e^+e^- collisions the fragmentation variable $x_p^{Breit} = 2|\vec{p}|/Q$ is defined, where \vec{p} is the momentum of the particle in the Breit frame; x_p^{Breit} corresponds to $x_p = p/p_{beam}$ in e^+e^- collider experiments. Strange quarks produced directly in the hard interaction are expected to preferentially populate the current hemisphere, which is less sensitive to non-perturbative strangeness contributions. In the case of baryon production the hemisphere separation is useful to study also baryon transfer, which is expected to be relevant at high x_p^{Breit} in the target frame.

2.2 Monte Carlo Simulation

The deep-inelastic ep interactions are simulated using the DJANGO program [12]. It generates hard partonic processes at Born level and at leading order in α_S (e.g. $\gamma^*q \rightarrow q$, $\gamma^*q \rightarrow qq$, $\gamma^*g \rightarrow q\bar{q}$), convoluted with the parton distribution function (PDF) for the proton, chosen herein to be CTEQ6L [13]. The factorisation and renormalisation scales are set to $\mu_f^2 = \mu_r^2 = Q^2$. Within DJANGO, higher order QCD effects are accounted for using either the parton shower approach as implemented in LEPTO [14] (referred to as MEPS) or by the so-called colour dipole model approach available within ARIADNE [15] (referred to as CDM [16]). In LEPTO, the parton showers are ordered in the transverse momenta (k_T) of emissions, according to the leading $\log(Q^2)$ approximation. In the ARIADNE program, the partons are generated by colour dipoles spanned between the partons in the cascade; since the dipoles radiate independently, there is no k_T ordering.

The hadronisation process is modelled according to the LUND colour string fragmentation model [10], as implemented in the JETSET [17] program. Within this model, the strange quark suppression is predominantly described by the (constant) factor $\lambda_s = P_s/P_q$, where P_s and P_q are the probabilities for creating strange (s) or light ($q = u$ or d) quarks in a non-perturbative process from the colour field during the fragmentation process. Further important parameters of this model are the diquark suppression factor $\lambda_{qq} = P_{qq}/P_q$, i.e. the probability of producing a light diquark pair $qq\bar{q}\bar{q}$ from the vacuum with respect to a light $q\bar{q}$ pair, and the strange diquark suppression factor $\lambda_{sq} = (P_{sq}/P_{qq})/(P_s/P_q)$, which models the relative production of strange diquark pairs. These are the two most relevant factors for the description of baryon production. The $s\bar{s}$ pair production rate is primarily dominated by λ_s , i.e. $u(\bar{u}) : d(\bar{d}) : s(\bar{s}) = 1 : 1 : \lambda_s$. The values tuned to hadron production measurements by the ALEPH collaboration [4] ($\lambda_s = 0.286$, $\lambda_{qq} = 0.108$, and $\lambda_{sq} = 0.690$) are taken herein as default values for the simulation of hadronisation within JETSET.

Previously published H1 and ZEUS data [8, 18] are better described by a lower value $\lambda_s = 0.2$. A recent ZEUS analysis [9] favours $\lambda_s = 0.3$ from cross section results and $\lambda_s = 0.22$ from

measurements of the strange mesons to charged hadrons ratio. The same theoretical framework is also used in e^+e^- analyses and thus allows for tests of strangeness suppression universality.

Monte Carlo event samples generated with DJANGO are used for the acceptance and efficiency correction of the data. All generated events are passed through the full GEANT [19] based simulation of the H1 apparatus and are reconstructed and analysed using the same programs as for the data.

3 Experimental Procedure

3.1 H1 Detector

A detailed description of the H1 detector can be found in [20]. In the following, only those detector components important for the present analysis are described. H1 uses a right handed Cartesian coordinate system with the origin at the nominal ep interaction point. The proton beam direction defines the positive z -axis of the laboratory frame and transverse momenta are measured in the $x - y$ plane. The polar angle θ is measured with respect to this axis and the pseudorapidity η is given by $\eta = -\ln \tan \frac{\theta}{2}$.

Charged particles are measured in the Central Tracking Detector (CTD) in the range $-1.75 < \eta < 1.75$. The CTD comprises two cylindrical Central Jet Chambers (CJCs), arranged concentrically around the beam-line, complemented by a silicon vertex detector (CST) [21], two z -drift chambers and two multi-wire proportional chambers for triggering purposes, all within a solenoidal magnetic field of strength 1.16 T. The transverse momentum resolution is $\sigma(p_T)/p_T \simeq 0.006 p_T / \text{GeV} \oplus 0.015$ [22]. In each event the tracks are used in a common fit procedure to determine the ep interaction vertex.

The tracking detectors are surrounded by a Liquid Argon calorimeter (LAr) in the forward and central region ($-1.5 < \eta < 3.4$) and by a lead-scintillating fibre calorimeter (SpaCal) in the backward region [23] ($-4 < \eta < -1.4$). The SpaCal is designed for the detection of scattered positrons in the DIS kinematic range considered here and has an electromagnetic energy resolution of $\sigma_E/E \simeq 7\%/\sqrt{E/\text{GeV}} \oplus 1\%$. The backward drift chamber (BDC), positioned in front of the SpaCal, improves the measurement of the positron polar angle and is used to reject neutral particle background. The DIS events studied in this paper are triggered by an energy deposition in the SpaCal, complemented by signals in the CJCs and in the multi-wire proportional chambers.

The luminosity is determined from the rate of the Bethe-Heitler process, $ep \rightarrow ep\gamma$, measured using a calorimeter located close to the beam pipe at $z = -103$ m.

3.2 Selection of DIS Events

The analysis is based on a data sample corresponding to an integrated luminosity of $\mathcal{L} = 49.9 \text{ pb}^{-1}$, recorded when HERA collided positrons at an energy $E_e = 27.6 \text{ GeV}$ with protons at 920 GeV in the years 1999 and 2000.

The selection of DIS events is based on the identification of the scattered positron as a compact calorimetric deposit in the SpaCal. The cluster radius is required to be less than 3.5 cm, consistent with an electromagnetic energy deposition. The cluster centre must be geometrically associated with a charged track candidate in the BDC. These conditions reduce background from photoproduction processes.

At fixed centre of mass energies \sqrt{s} the kinematics of the scattering process are described using the Lorentz invariant variables Q^2 , y and x . These variables can be expressed as a function of the scattered positron energy E'_e and its scattering angle θ_e in the laboratory frame:

$$Q^2 = 4E_e E'_e \cos^2\left(\frac{\theta_e}{2}\right), \quad y = 1 - \frac{E'_e}{E_e} \sin^2\left(\frac{\theta_e}{2}\right), \quad x = \frac{Q^2}{ys}. \quad (1)$$

The negative four-momentum transfer squared Q^2 and the inelasticity y are required to lie in the ranges $2 < Q^2 < 100 \text{ GeV}^2$ and $0.1 < y < 0.6$. Background from events at low Q^2 , in which the electron escapes undetected down the beam pipe and a hadron fakes the electron signature, is suppressed by the requirement that the difference $\Sigma(E - p_z)$ between the total energy and the longitudinal momentum must be in the range $35 < \Sigma(E - p_z) < 70 \text{ GeV}$, where the sum includes all measured hadronic final state particles and the scattered electron candidate. Events are accepted if the z -coordinate of the event vertex, reconstructed using the tracking detectors, lies within $\pm 35 \text{ cm}$ of the mean position for ep interactions.

3.3 Selection of Hadron Candidates

The neutral strange K_s^0 meson and Λ baryon states¹ are measured by the kinematic reconstruction of their decays $K_s^0 \rightarrow \pi^+\pi^-$ and $\Lambda \rightarrow p\pi^-$. The analysis is based on charged particles measured in the central region of the H1 detector with a minimum transverse momentum $p_T \geq 0.12 \text{ GeV}$. The neutral strange hadrons K_s^0 and Λ are identified by fitting pairs of oppositely charged tracks in the $x - y$ plane to their secondary decay vertices, with the direction of flight of the mother particle constrained to the primary event vertex. K_s^0 and Λ candidates are retained if the fit probability is above 1%. In order to reduce background, the radial distance L of the secondary vertex to the beam line is required to be larger than 5 mm and the vertex separation significance $L/\sigma_L > 4$, where σ_L is the uncertainty of L . The transverse momentum and the pseudorapidity of the K_s^0 (Λ) candidates are required to satisfy $0.5 < p_T < 3.5 \text{ GeV}$ and $|\eta| < 1.3$. A detailed description of the analyses can be found in [24, 25].

For K_s^0 candidate reconstruction both tracks are assumed to be pions, while for the Λ reconstruction the track with the higher momentum is assumed to be the proton and the other track is assumed to be the pion. The contamination from Λ (K_s^0) decays in K_s^0 (Λ) candidates is suppressed by a rejection of the corresponding invariant mass region: $|M(\pi p) - m_\Lambda| > 6 \text{ MeV}$ for the K_s^0 and $|M(\pi\pi) - m_{K_s^0}| > 10 \text{ MeV}$ for the Λ selection. The Λ ($\bar{\Lambda}$) baryons are tagged by the electrical charge of the decay proton (antiproton). The invariant mass spectra $M(\pi^+\pi^-)$ and $M(p\pi)$ of all candidates passing these criteria are shown in figures 2 and 3, respectively.

¹Unless explicitly mentioned, a reference to a state implicitly includes the charge conjugate of that state.

The number of signal particles N_S is obtained by fitting the invariant mass spectra with the sum of a signal and a background function. The signal function S has the same shape for K_s^0 and Λ and is composed of two Gaussian functions of identical central value μ and of different widths σ_1 and σ_2 that account for different resolution effects. The background functions $B_{K_s^0}(M)$ and $B_\Lambda(M)$ are chosen with different shapes for the K_s^0 and Λ cases. These functions are defined according to

$$S(M) = P_0 \cdot G(N_S, \mu, \sigma_1) + (1 - P_0) \cdot G(N_S, \mu, \sigma_2), \quad (2)$$

$$B_{K_s^0}(M) = P_1 + P_2 \cdot M, \quad (3)$$

$$B_\Lambda(M) = P_1 \cdot (M - m_\Lambda)^{P_2} \cdot e^{(1+P_3 \cdot M + P_4 \cdot M^2)}. \quad (4)$$

Here, M denotes the $\pi\pi$ and the $p\pi$ invariant mass, respectively, and m_Λ the nominal mass of the Λ baryon [26]. The normalisation N_S , the central value μ , the widths σ_1 and σ_2 of the Gaussian function G and the parameters P_i are left free in the fit. P_0 represents the relative normalisation of the two signal Gaussians. For the differential distributions the fit is repeated in each of the kinematic bins.

The fit yields approximately 213000 K_s^0 mesons. The fitted mass of 496.9 ± 0.1 (stat.) MeV is consistent with the world average [26] and the measured mean width 13.8 ± 0.4 (stat.) MeV is described by the simulated detector resolution within 20%. In the case of the Λ the fit yields approximately 22000 Λ and 20000 $\bar{\Lambda}$ baryons. The fitted mass of 1115.8 ± 0.1 (stat.) MeV is also consistent with the world average [26] and the measured width of 4.3 ± 0.3 (stat.) MeV is consistent with the detector resolution within 20%.

Charged hadrons h^\pm used for the ratio $R(K_s^0/h^\pm)$ are defined as long-lived particles with a lifetime $> 10^{-8}$ s detected in the same kinematic region as strange particles ($|\eta| < 1.3$, $0.5 < p_T < 3.5$ GeV), with the following additional requirements: each track must point to the primary vertex, the number of associated hits in the CJC must be greater than eight, the radial track length must be longer than 10 cm and the radial distance from the beam line to the innermost hit associated with the track must be less than 50 cm.

4 Results

4.1 Determination of Cross Sections

The total inclusive cross section σ_{vis} in the accessible kinematic region is given by the following expression:

$$\sigma_{vis}(ep \rightarrow e[K_s^0, \Lambda, h^\pm]X) = \frac{N}{\mathcal{L} \cdot \epsilon \cdot BR \cdot (1 + \delta_{rad})}, \quad (5)$$

where N represents the observed number of K_s^0 , the sum of Λ and $\bar{\Lambda}$ baryons or the charged hadrons h^\pm , respectively. \mathcal{L} denotes the integrated luminosity. The branching ratios BR for the K_s^0 and Λ decays are taken from [26] and $BR = 1$ for charged hadrons. The number of K_s^0 and Λ particles are determined by fitting the mass distributions as explained in section 3.3. In the case of differential distributions the same formula is applied in each bin.

The efficiency ϵ is given by $\epsilon = \epsilon_{rec} \cdot \epsilon_{trig}$, where ϵ_{rec} is the reconstruction efficiency and ϵ_{trig} is the trigger efficiency. The reconstruction efficiency is estimated using CDM Monte Carlo event samples for the kinematic region and the visible range defined in sections 3.2 and 3.3, and amounts to 33.3 % and 19.5 % for the K_s^0 mesons and the Λ baryons, respectively. These numbers include the geometric acceptance and the efficiency for track and secondary vertex reconstruction. The geometric acceptance to find both decay particles in the CTD is about 80 % for the K_s^0 mesons and 70 % for the Λ baryons, respectively

The trigger efficiency is extracted from the data using monitor triggers and amounts to 81.5 % and 83.3 % for the K_s^0 and the Λ , respectively. The radiative correction δ_{rad} corrects the measured cross section to the Born level and is calculated using the program HERACLES [27]. It amounts to $\delta_{rad} = 6.6(4.3)$ % for the K_s^0 (Λ) on average and varies between -8% and $+19\%$ over the kinematic range considered. The trigger efficiency and radiative corrections are assumed to be the same for particles and antiparticles.

In the case of charged hadrons h^\pm , the reconstruction efficiency ϵ_{rec} is defined such that it includes corrections for K_s^0 and Λ decays, secondary interactions, photon conversions and the track reconstruction efficiency. The total correction $\epsilon(1 + \delta_{rad})$ amounts to 81.1%.

4.2 Systematic Uncertainties

The systematic uncertainties are studied using the CDM Monte Carlo simulation, unless otherwise stated. For the inclusive cross sections, the resulting systematic uncertainties are summarised in table 1. For the differential cross sections, the systematic uncertainties are estimated in each bin. The following contributions are considered:

- The energy scale in the Spacal measurements is known to 1 %, except for the lowest Q^2 bin ($2 < Q^2 < 2.5 \text{ GeV}^2$) where the uncertainty on the energy measurement is 2.5 %.
- The uncertainty of the measurement of the polar angle of the scattered positron is 1 mrad.
- The uncertainty on the overall number of reconstructed K_s^0 and Λ particles is determined from data by comparing the numbers obtained from the fit of the mass spectra with the number obtained by simply counting the events within $\pm 6\sigma$ of the nominal mass after subtracting the expected background. The number of background events is estimated by integrating the background function described in equation 4 over the corresponding interval ($0.42 - 0.58 \text{ GeV}$ for K_s^0 and $1.085 - 1.2$ for Λ). The procedure is cross checked by performing the fit in different mass ranges.
- The uncertainty of the reconstruction efficiency is determined by comparing its estimation using different models. The uncertainty is taken as 50 % of the difference between the CDM and the MEPS Monte Carlo simulations.
- The uncertainty on the trigger efficiency is obtained by comparing estimates using different monitor triggers (MT).
- The uncertainty on the luminosity measurement is 1.5 %.

- The uncertainty of the charged hadron reconstruction is 2% per track. For the measurement of the Λ to K_s^0 ratio the uncertainty caused by the pion track appearing in both decays is assumed to cancel. The systematic uncertainty on the ratio K_s^0/h^\pm is estimated to be 2.0%.
- The uncertainty due to the decay branching ratios is taken as 0.8% for Λ and is negligible for K_s^0 [26].

Source	Variation	$\Delta\sigma(K_s^0)$ [%]	$\Delta\sigma(\Lambda)$ [%]	$R(\Lambda/K_s^0)$ [%]	$R(K_s^0/h^\pm)$ [%]
E'_e	$\pm 1\%$	+3.3 -3.5	+2.8 -3.1	—	—
θ_e	± 1 mrad	± 1.4	± 1.5	—	—
signal extraction	$\frac{N^{fit} - N^{count}}{N^{fit}}$	± 0.6	± 1.4	± 1.5	± 0.6
model	$0.5 * \frac{\epsilon_{rec}^{CDM} - \epsilon_{rec}^{MEPS}}{\epsilon_{rec}^{CDM}}$	± 0.4	± 1.2	± 1.2	± 3.5
trigger efficiency	$\frac{\epsilon_{trig}^{MTset1} - \epsilon_{trig}^{MTset2}}{\epsilon_{trig}^{MTset1}}$	+0.4 -0.9	+1.0 -1.4	+1.1 -1.6	+0.4 -1.0
luminosity		± 1.5	± 1.5	—	—
track reco.	2.0% per track	± 4.0	± 4.0	± 2.0	± 2.0
branching ratio		± 0.1	± 0.8	± 0.8	± 0.1
Total systematic uncertainty		+5.6 -5.8	+5.8 -6.0	+3.1 -3.3	+4.1 -4.2

Table 1: Systematic sources, variations and corresponding relative errors of the inclusive cross sections and of the ratios of Λ to K_s^0 and K_s^0 to charged hadrons. All relative errors are expressed as percentages.

The systematic errors due to these uncertainties are estimated by varying each quantity within its error in the Monte Carlo simulation and repeating the cross section measurement. In the cross section calculation, the contributions are added in quadrature and included in the uncertainty shown in the individual bins of the differential distributions. In the ratios, the uncertainties on the electron energy scale and polar angle, as well as the luminosity, cancel. The other sources of uncertainty are assumed to be uncorrelated and are added in quadrature.

4.3 Inclusive Production Measurements

The inclusive K_s^0 , Λ and charged hadron h^\pm production cross sections σ_{vis} are measured in the kinematic region $2 < Q^2 < 100 \text{ GeV}^2$ and $0.1 < y < 0.6$, for the ranges $0.5 < p_T(K_s^0, \Lambda, h^\pm) < 3.5 \text{ GeV}$ and $|\eta(K_s^0, \Lambda, h^\pm)| < 1.3$.

The K_s^0 cross section is found to be

$$\sigma_{vis}(ep \rightarrow eK_s^0 X) = 21.18 \pm 0.09(\text{stat.})_{-1.23}^{+1.19}(\text{syst.}) \text{ nb.} \quad (6)$$

The measurement is in agreement with the expectation 21.77 nb based on the LO Monte Carlo program DJANGO, using the CDM approach and the default value of $\lambda_s = 0.286$.

The cross section for the sum of Λ and $\bar{\Lambda}$ baryon production is measured in the same kinematic region and is found to be

$$\sigma_{vis}(ep \rightarrow e[\Lambda + \bar{\Lambda}]X) = 7.88 \pm 0.10(\text{stat.})_{-0.47}^{+0.45}(\text{syst.}) \text{ nb,} \quad (7)$$

in agreement with the expectation of 7.94 nb from the DJANGO calculation. The individual Λ and $\bar{\Lambda}$ production rates are measured to be

$$\sigma_{vis}(ep \rightarrow e\Lambda X) = 3.96 \pm 0.06(\text{stat.})_{-0.24}^{+0.23}(\text{syst.}) \text{ nb,} \quad (8)$$

$$\sigma_{vis}(ep \rightarrow e\bar{\Lambda} X) = 3.94 \pm 0.07(\text{stat.})_{-0.24}^{+0.23}(\text{syst.}) \text{ nb,} \quad (9)$$

and are therefore found to be consistent with each other within the statistical precision. The measurements are also in agreement with the DJANGO prediction of 3.97 nb. The systematic errors are fully correlated.

The inclusive ratio of strange baryon to meson production is determined to be

$$\frac{\sigma_{vis}(ep \rightarrow e[\Lambda + \bar{\Lambda}]X)}{\sigma_{vis}(ep \rightarrow eK_s^0 X)} = 0.372 \pm 0.005(\text{stat.})_{-0.012}^{+0.011}(\text{syst.}), \quad (10)$$

in agreement with the prediction of 0.365 from the DJANGO calculation.

The ratio of cross sections of K_s^0 mesons to charged hadrons h^\pm is found to be

$$\frac{\sigma_{vis}(ep \rightarrow eK_s^0 X)}{\sigma_{vis}(ep \rightarrow eh^\pm X)} = 0.0645 \pm 0.0002(\text{stat.})_{-0.0020}^{+0.0019}(\text{syst.}), \quad (11)$$

in agreement with the DJANGO prediction of 0.0638 based on MEPS with $\lambda_s = 0.22$. Similar values of 0.05 – 0.07 are obtained for the ratio of the average K_s^0 multiplicity over the average charged pion multiplicity in e^+e^- annihilation events at centre of mass energies from 10 to 200 GeV [26].

4.4 Differential Production Cross Sections

Production cross sections and ratios of K_s^0 , Λ and charged hadrons h^\pm are measured in the visible kinematic region differentially in the event variables Q^2 and x and in the laboratory frame variables p_T and η . Differential cross sections are also measured as a function of the variables x_p^{Breit} and p_T^{Breit} defined in the Breit frame. The results are bin-averaged and no bin-centre corrections are applied. The distributions are shown in figures 4 to 13 and are compared with the predictions. The numerical values are also listed in tables 2 to 8.

4.4.1 Discussion of K_s^0 and Λ Results

The measured differential cross sections of K_s^0 and Λ production are shown in figures 4 to 7 and listed in tables 2 to 5. The cross sections decrease rapidly as a function of Q^2 and x , similarly to the inclusive DIS distributions. The cross sections are also observed to fall rapidly with p_T .

In the laboratory frame the overall features of the distributions are reproduced by the DJANGO simulations at the level of 10 to 20%. For comparison, the CDM and MEPS model predictions are each given with two values of the suppression factor $\lambda_s = 0.3$ and $\lambda_s = 0.22$. The predictions based on the CDM model with $\lambda_s = 0.3$ provide a reasonably good description of the data for K_s^0 and Λ production. The MEPS simulation produces distributions, which are quite similar in shape to the CDM model predictions but with a different normalisation in the case of K_s^0 production, where a lower value of $\lambda_s = 0.22$ describes the data better. In the case of Λ production, both MEPS and CDM predictions are very similar in shape and normalisation and $\lambda_s = 0.3$ provides a better description of the data. For these comparisons, only the parameter λ_s is varied to describe the data. However, in contrast to the K_s^0 , the Λ production cross sections also depend significantly on the JETSET parameters that describe diquark and strange diquark creation.

The cross sections measured as a function of x_p^{Breit} and p_T^{Breit} in the Breit frame are shown in figures 6 and 7 and listed in tables 4 and 5, for both the target and the current region. The cross section values in the target regions are about one order of magnitude higher than in the current region. They are generally well described by both the MEPS and CDM model predictions. The predicted momentum distributions tend to be softer than in the data. However, in the current region the sensitivity to λ_s is clearly reduced with respect to the laboratory frame or the target region. This is due to both larger errors and an increased fraction of strangeness produced in perturbative processes, which contributes up to about 50% (compared to about 25% in the target hemisphere).

To test the mechanism of baryon number transfer, the asymmetry in the production of Λ with respect to $\bar{\Lambda}$ is measured by the variable

$$A_\Lambda = \frac{\sigma_{vis}(ep \rightarrow e\Lambda X) - \sigma_{vis}(ep \rightarrow e\bar{\Lambda} X)}{\sigma_{vis}(ep \rightarrow e\Lambda X) + \sigma_{vis}(ep \rightarrow e\bar{\Lambda} X)}. \quad (12)$$

A significant $\Lambda - \bar{\Lambda}$ asymmetry $A_\Lambda \neq 0$ would indicate a transfer of the baryon number from the proton beam to the final state strange particles. The measured distributions of A_Λ in the laboratory and Breit frames are shown in figures 8 and 9, respectively. All distributions are observed to be compatible with zero within errors. Thus, no evidence of baryon number transfer is visible in the measured $\Lambda/\bar{\Lambda}$ data.

In order to test for possible dependencies of strange hadron production on the proton parton density functions, the measured distributions are compared with different PDF parametrisations. Figure 10 shows the differential cross sections for K_s^0 and Λ production compared with the CDM predictions using the CTEQ6L [13], H12000LO [28] and GRV LO [29] parametrisations and $\lambda_s = 0.286$. The predictions of the Q^2 dependence of the cross section are notably different for different PDFs for both the K_s^0 and the Λ . The p_T distributions indicate only a slight dependence while the η distributions do not exhibit any PDF dependence. The small discrepancy in the forward direction is not resolved by different PDF parametrisations. Similar results are obtained in the Breit frame.

4.4.2 Ratios of Production Cross Sections

Different aspects of baryon production within the fragmentation models can be tested with reduced theoretical uncertainties by studying the ratio of the differential cross sections for Λ baryons and K_s^0 mesons $R(\Lambda/K_s^0) = d\sigma(ep \rightarrow e\Lambda X) / d\sigma(ep \rightarrow eK_s^0 X)$. The measurements are shown in figures 11 and 12 and listed in tables 6 and 7. The CDM implementation provides a reasonably good description of the data in the laboratory frame (figure 11), although systematic deviations are seen at high Q^2 and in the shape of the η distribution, whereas the MEPS predictions clearly underestimate the data. The model predictions are not sensitive to λ_s , as expected.

The dependence of $R(\Lambda/K_s^0)$ on p_T^{Breit} and x_p^{Breit} (figure 12) are reasonably well described in both the target and current hemispheres. The predictions are almost independent of the model implementation (CDM, MEPS) and the λ_s values used.

The ratio of differential production cross sections for K_s^0 mesons and charged hadrons, denoted by $R(K_s^0/h^\pm) = d\sigma(ep \rightarrow eK_s^0 X) / d\sigma(ep \rightarrow eh^\pm X)$, is equivalent to the ratio of the average multiplicities of K_s^0 and charged hadrons. In contrast to inclusive K_s^0 production, the correlation of $R(K_s^0/h^\pm)$ to the parameter λ_s is expected to be less model dependent. By taking the ratio, inadequacies of the model description of the partonic final states and in particular of the dependence on the proton structure function should cancel to a large extent. The ratio $R(K_s^0/h^\pm)$ is shown in figure 13 and listed in table 8 as a function of Q^2 , x , p_T and η . The ratio strongly rises with increasing p_T and remains approximately constant as a function of all the other variables. This p_T dependence of $R(K_s^0/h^\pm)$ reflects a general kinematic feature (heavier particles receive the larger fraction of the system momentum) and can also be observed in the Λ/K_s^0 ratio in figure 11.

Also shown with the data are the CDM and MEPS model predictions for two values of λ_s (0.22 and 0.3). Overall, no single prediction is able to fully describe the shapes of all $R(K_s^0/h^\pm)$ distributions, failing in particular in the low p_T , low x and large positive η regions. The p_T spectrum of $R(K_s^0/h^\pm)$ is found to be harder in the data, consistent with the conclusions derived from the cross section measurement.

The shapes of the ratios $R(K_s^0/h^\pm)$ are reasonably described by both CDM and MEPS model predictions. However, there is a difference in normalisation between the two models. The CDM prediction with $\lambda_s = 0.3$ is in better agreement with the data at low Q^2 , whereas at high Q^2 a value of $\lambda_s = 0.22$ is preferred, as observed in the ZEUS data [9]. In contrast, the MEPS model predictions prefer a lower value of $\lambda_s = 0.22$ over the full phase space.

A comparison of the predictions, applying different settings for the diquark-quark suppression factors ($\lambda_{qq}, \lambda_{sq}$) shows the expected behaviour. In general, no changes are visible in the shapes of the differential distributions, however some differences are present in the absolute normalisation. The K_s^0 distributions are not affected, as expected, and both the Λ and the ratio $R(\Lambda/K_s^0)$ show the anticipated correlations to the suppression factors ($\lambda_{qq}, \lambda_{sq}$). These predicted effects are mostly independent of the choice of the λ_s value, used for the simulation, and indicate that the ‘‘ALEPH-tune’’ from e^+e^- collisions also describes the overall features of the data in ep collisions, supporting the universality of strangeness production.

5 Conclusions

The production cross sections and ratios of the production of K_s^0 , Λ and charged hadrons h^\pm are measured inclusively and also differentially as a function of the DIS variables and of the final state particle variables in the visible kinematic region, defined by $2 < Q^2 < 100 \text{ GeV}^2$, $0.1 < y < 0.6$, $0.5 < p_T(K_s^0, \Lambda, h^\pm) < 3.5 \text{ GeV}$ and $|\eta(K_s^0, \Lambda, h^\pm)| < 1.3$.

The measured total cross sections and their ratios are in agreement with the predictions based on DJANGO. The overall features of the various differential distributions are reasonably well reproduced by both simulations, based either on the CDM or the MEPS approach, when applying model parameters obtained from e^+e^- data at LEP. However, predictions based on a single value of λ_s fail to describe the details of the distributions in various regions of the phase space, in particular in the low p_T , low x and large positive η regions. The production of K_s^0 and Λ particles, as measured in the Breit frame, is in general described by both CDM and MEPS predictions. The measurement of the asymmetry in the production of Λ with respect to $\bar{\Lambda}$, which is found to be consistent with zero within errors, does not support the hypothesis of baryon number transfer.

The Λ to K_s^0 cross section ratio is better described by the CDM prediction and is nearly independent of the λ_s value, whereas for the K_s^0 to charged hadrons cross section ratio the MEPS model with $\lambda_s = 0.22$ is in better agreement with the data.

Acknowledgements

We are grateful to the HERA machine group whose outstanding efforts have made this experiment possible. We thank the engineers and technicians for their work in constructing and maintaining the H1 detector, our funding agencies for financial support, the DESY technical staff for continual assistance and the DESY directorate for support and for the hospitality which they extend to the non DESY members of the collaboration.

References

- [1] M. Althoft *et al.* [TASSO Collaboration], *Z. Phys. C* **27** (1985) 27.
- [2] P. D. Acton *et al.* [OPAL Collaboration], *Phys. Lett. B* **291** (1992) 503;
G. Alexander *et al.* [OPAL Collaboration], *Z. Phys. C* **73** (1997) 569.
- [3] K. Abe *et al.* [SLD Collaboration], *Phys. Rev. D* **59** (1999) 052001.
- [4] R. Barate *et al.* [ALEPH Collaboration], *Phys. Rept.* **294** (1998) 1.
- [5] P. Abreu *et al.* [DELPHI Collaboration], *Z. Phys. C* **73** (1996) 11.
- [6] B. Kopeliovich and B. Povh, *Z. Phys. C* **75** (1997) 693 [hep-ph/9607486].
- [7] M. Arneodo *et al.* [EMC Collaboration], *Z. Phys. C* **34** (1987) 283.
- [8] S. Aid *et al.* [H1 Collaboration], *Nucl. Phys. B* **480** (1996) 3 [hep-ex/9607010].
- [9] S. Chekanov *et al.* [ZEUS Collaboration], *Eur. Phys. J. C* **51** (2007) 1 [hep-ex/0612023].
- [10] T. Sjöstrand, *Comput. Phys. Commun.* **39** (1986) 347;
T. Sjöstrand and M. Bengtsson, *Comput. Phys. Commun.* **43** (1987) 367;
B. Andersson *et al.* *Phys. Rept.* **97** (1983) 31.
- [11] R. P. Feynman, "Photon-Hadron Interactions", Benjamin, N.Y. (1972).
- [12] G. A. Schuler and H. Spiesberger, in *Proc. of the Workshop on HERA Physics*, edited by W. Büchmüller and G. Ingelman, DESY, Hamburg, 1992, vol.3, p.1419.
- [13] J. Pumplin *et al.* *JHEP* **0207** (2002) 012 [hep-ph/0201195].
- [14] G. Ingelman *et al.* *Comput. Phys. Commun.* **101** (1997) 108 [hep-ph/9605286].
- [15] L. Lönnblad, Ariadne version 4, *Comput. Phys. Commun.* **71** (1992) 15.
- [16] B. Andersson *et al.* *Z. Phys. C* **43** (1989) 625;
L. Lönnblad, *Z. Phys. C* **65** (1995) 285.
- [17] T. Sjöstrand, *Comput. Phys. Commun.* **82** (1994) 74, JETSET version 7.4 is used.
- [18] M. Derrick *et al.* [ZEUS Collaboration], *Z. Phys. C* **68** (1995) 29 [hep-ex/9505011].
- [19] R. Brun *et al.* GEANT3, Technical Report CERN-DD/EE/84-1, CERN, 1987.
- [20] I. Abt *et al.* [H1 Collaboration], *Nucl. Instrum. Meth. A* **386** (1997) 310;
I. Abt *et al.* [H1 Collaboration], *Nucl. Instrum. Meth. A* **386** (1997) 348.
- [21] D. Pitzl *et al.* *Nucl. Instrum. Meth. A* **454** (2000) 334 [hep-ex/0002044].
- [22] C. Kleinwort, "H1 Alignment Experience" in *Proc. of the First LHC Detector Alignment Workshop*, edited by S. Blusk *et al.* CERN-2007-004, p.41.

- [23] R. D. Appuhn *et al.* [H1 SPACAL Group], Nucl. Instrum. Meth. A **386** (1997) 397.
- [24] M. Del Degan, "Spectroscopy in ep Scattering at HERA". Ph.D. thesis, ETH Zurich, (2008) (in preparation, to appear at <http://www-h1.desy.de/psfiles/theses/>).
- [25] A. Falkiewicz, "Strangeness Production in Deep-Inelastic ep Collisions in H1 Experiment at HERA" (in Polish), Ph.D. thesis, Institute of Nuclear Physics PAS Krakow (2008) (in preparation, to appear at <http://www-h1.desy.de/psfiles/theses/>).
- [26] W. M. Yao *et al.* [Particle Data Group], J. Phys. G **33** (2006) 1.
- [27] A. Kwiatkowski, H. Spiesberger and H. J. Möhring, HERACLES version 1.0, Comput. Phys. Commun. **69** (1992) 155.
- [28] C. Adloff *et al.* [H1 Collaboration], Eur. Phys. J. C **30** (2003) 1 [hep-ex/0304003].
- [29] M. Glück, E. Reya and A. Vogt, Z. Phys. C **67** (1995) 433.

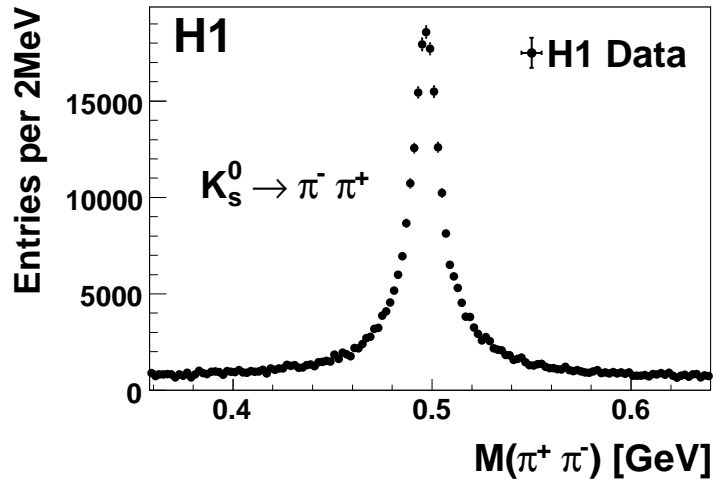


Figure 2: The invariant mass spectrum for $\pi^+ \pi^-$ particle combinations. The data are shown with error bars denoting the statistical uncertainty.

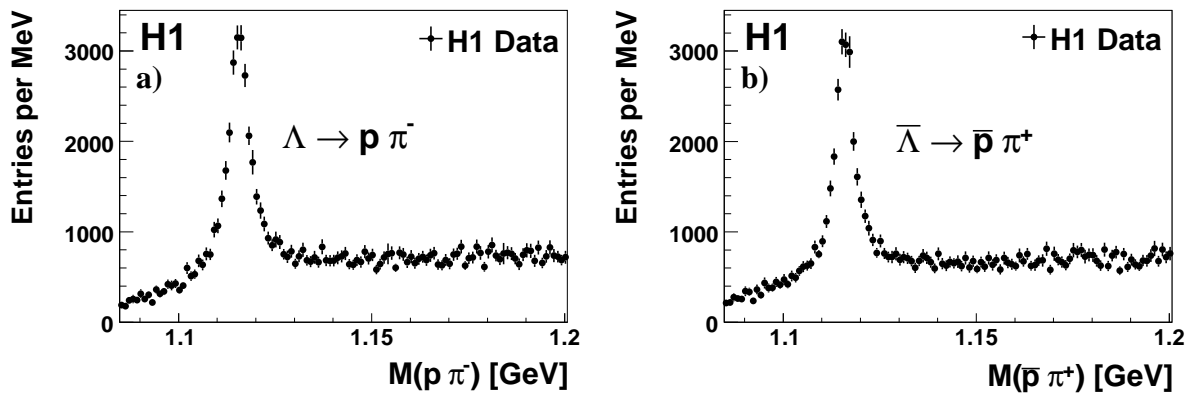


Figure 3: The invariant mass spectra for a) $\Lambda \rightarrow p \pi^-$ and b) $\bar{\Lambda} \rightarrow \bar{p} \pi^+$ particle combinations. The data are shown with error bars denoting the statistical uncertainty.

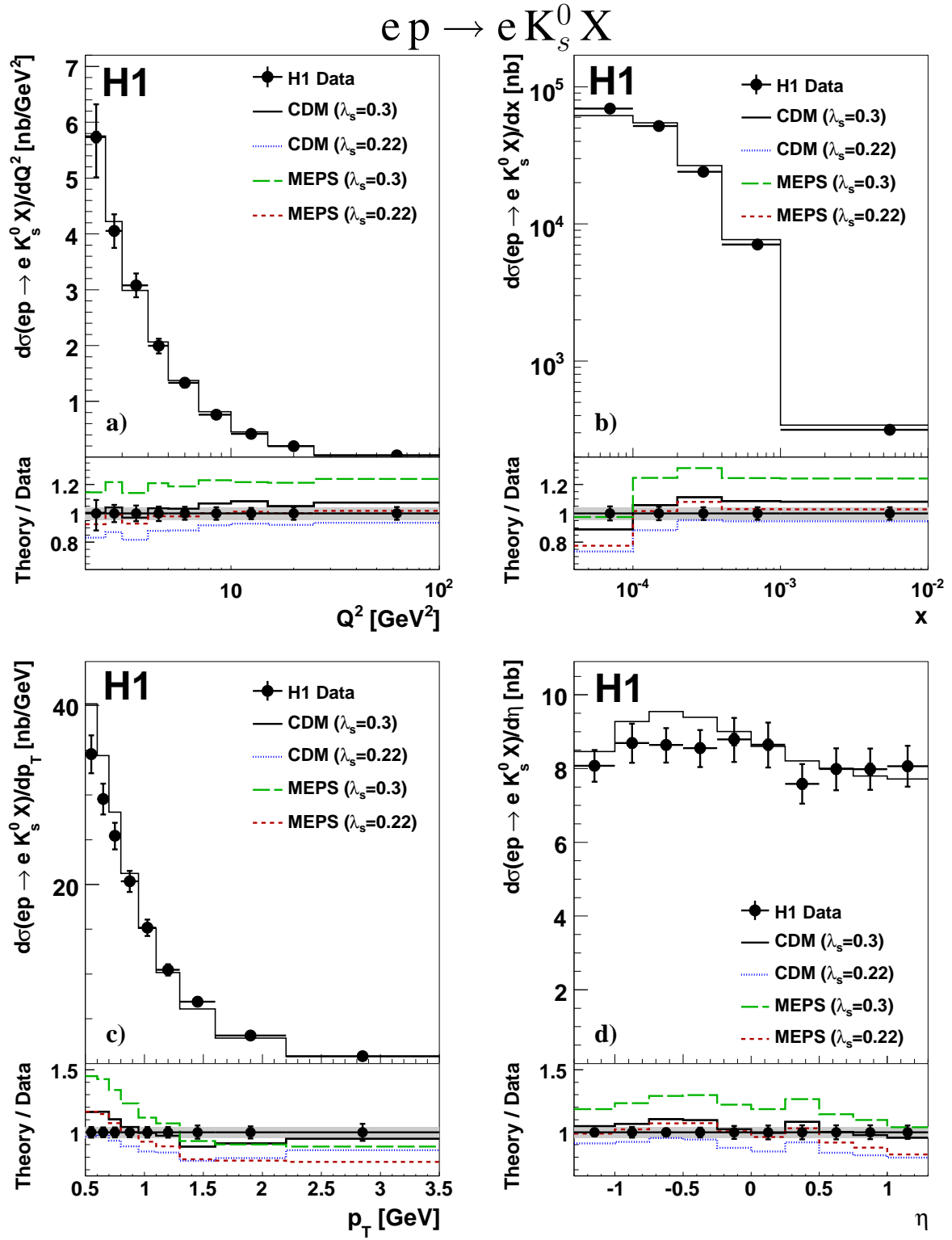


Figure 4: The differential production cross sections for K_s^0 in the laboratory frame as a function of the a) photon virtuality squared Q^2 , b) Bjorken scaling variable x , c) K_s^0 transverse momentum p_T and d) K_s^0 pseudorapidity η . The inner (outer) error bars show the statistical (total) errors. On the bottom of each figure, the “Theory/Data” ratios are shown for different LO Monte Carlo predictions (see text). For comparison, the data points are put to one and only uncorrelated errors are shown; the correlated systematic errors are indicated by the grey band.

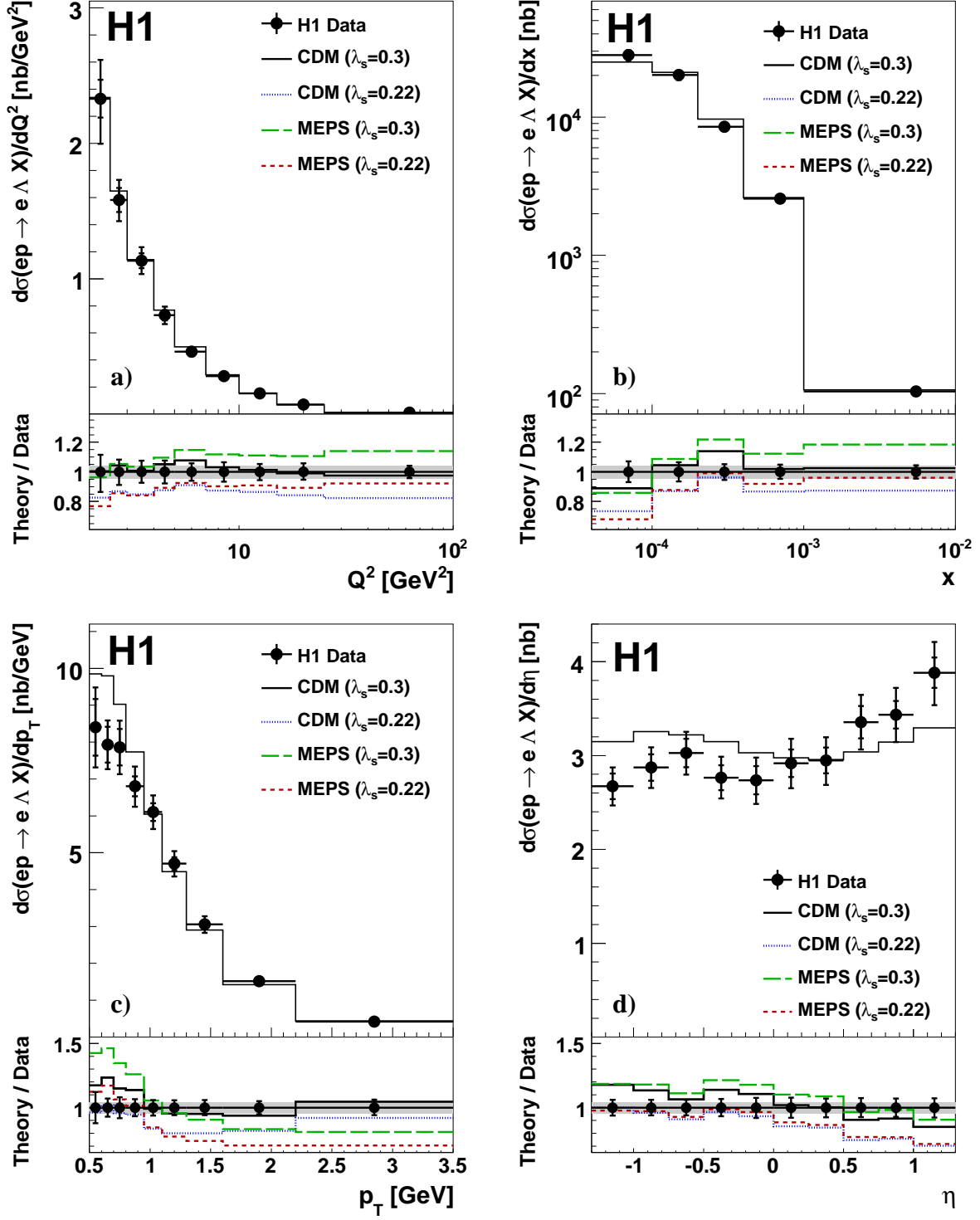
$$ep \rightarrow e \Lambda X$$


Figure 5: The differential production cross sections for Λ in the laboratory frame as a function of the a) photon virtuality squared Q^2 , b) Bjorken scaling variable x , c) Λ transverse momentum p_T and d) Λ pseudorapidity η . More details in the caption of figure 4.

$e p \rightarrow e K_s^0 X$ (Breit frame)

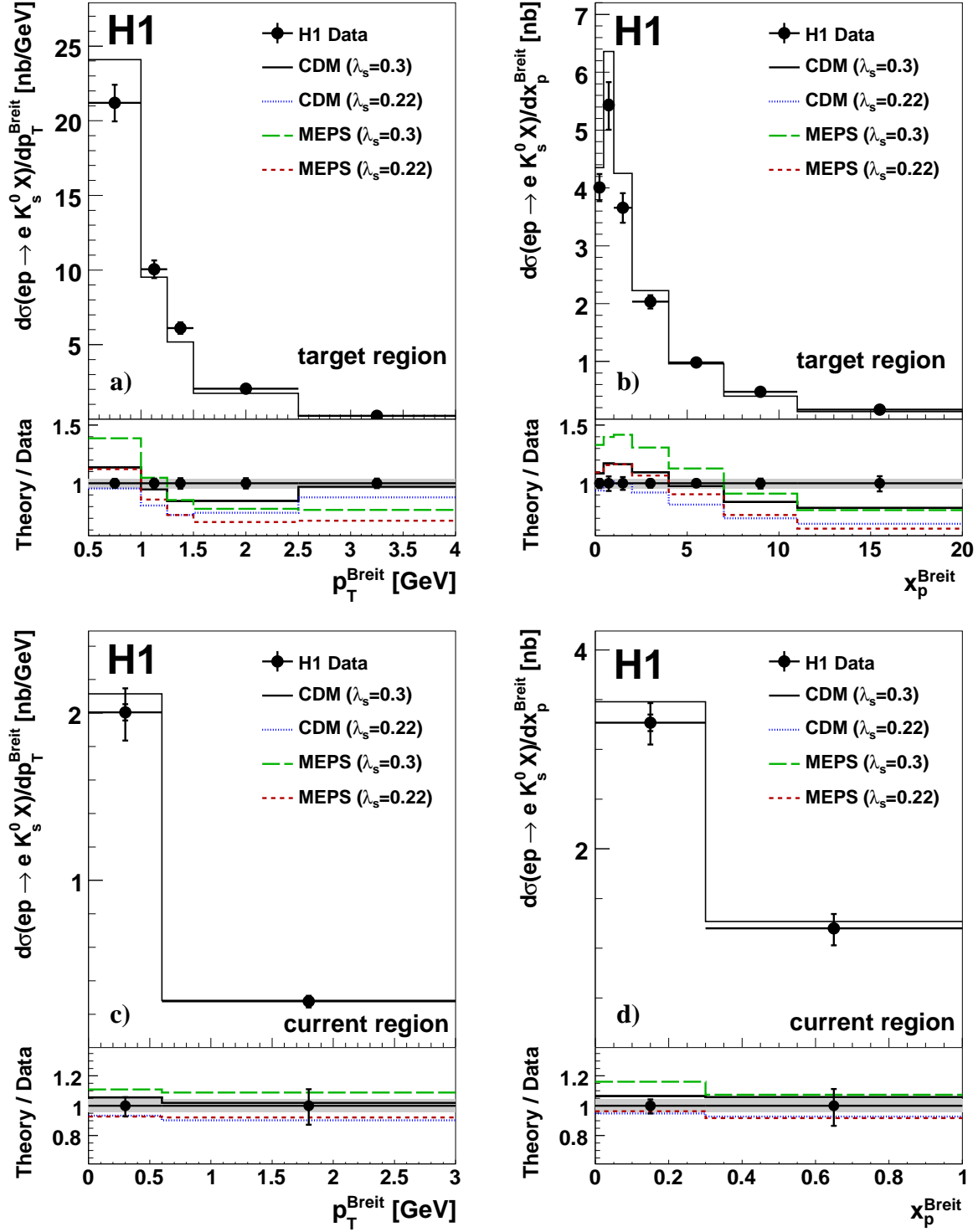


Figure 6: The differential K_s^0 production cross sections in the Breit frame as a function of K_s^0 transverse momentum p_T^{Breit} and momentum fraction x_p^{Breit} in the target hemisphere (a, b) and in the current hemisphere (c, d). More details in the caption of figure 4.

$e p \rightarrow e \Lambda X$ (Breit frame)

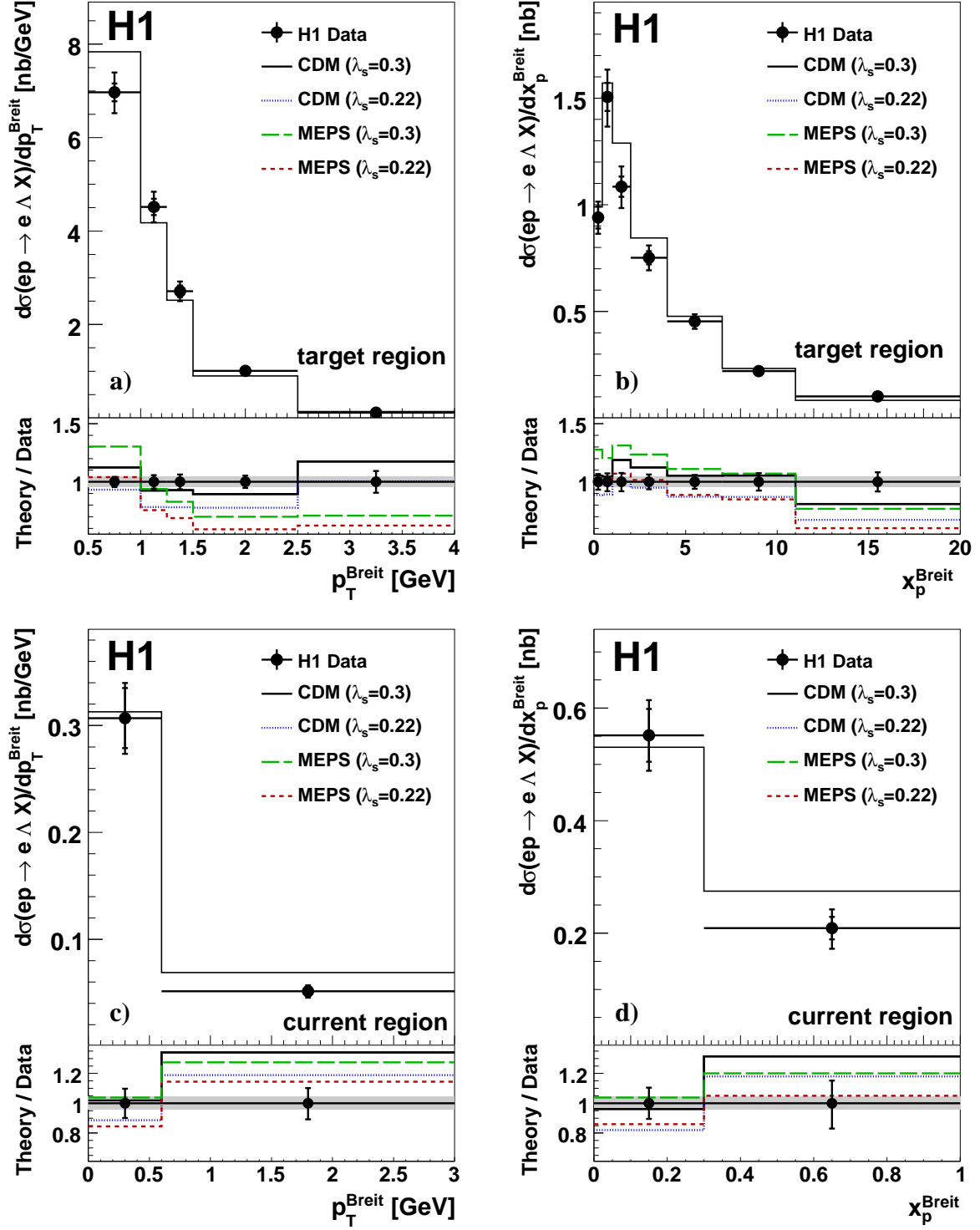


Figure 7: The differential production cross sections for the Λ baryons measured in the Breit frame as a function of Λ transverse momentum p_T^{Breit} and momentum fraction x_p^{Breit} in the target hemisphere (a, b) and in the current hemisphere (c, d). More details in the caption of figure 4.

$\Lambda - \bar{\Lambda}$ Asymmetry

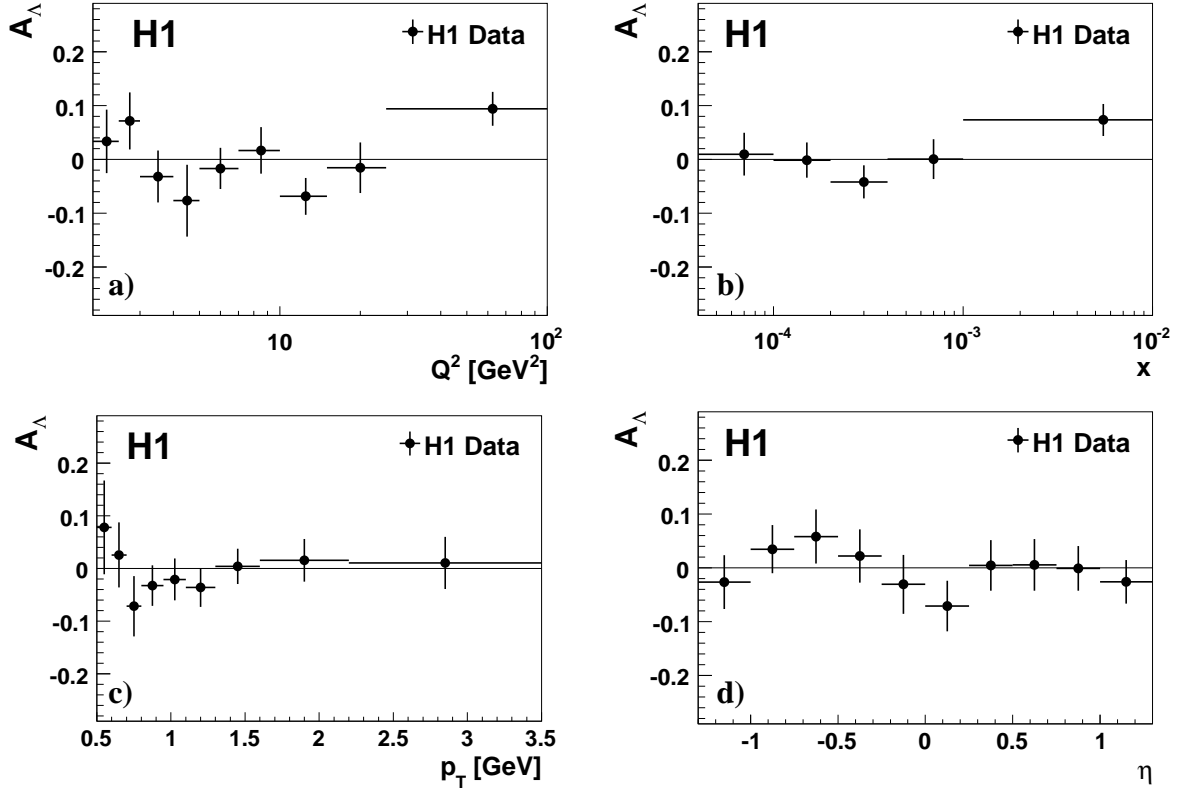


Figure 8: The asymmetry A_Λ of the differential production cross sections of the Λ and $\bar{\Lambda}$ baryons in the laboratory frame as a function of the a) photon virtuality squared Q^2 , b) Bjorken scaling variable x , c) transverse momentum p_T and d) pseudorapidity η . The asymmetry is defined as $A_\Lambda = [\sigma_{vis}(ep \rightarrow e\Lambda X) - \sigma_{vis}(ep \rightarrow e\bar{\Lambda} X)] / [\sigma_{vis}(ep \rightarrow e\Lambda X) + \sigma_{vis}(ep \rightarrow e\bar{\Lambda} X)]$. The error bars show the statistical uncertainty.

$\Lambda - \bar{\Lambda}$ Asymmetry (Breit frame)

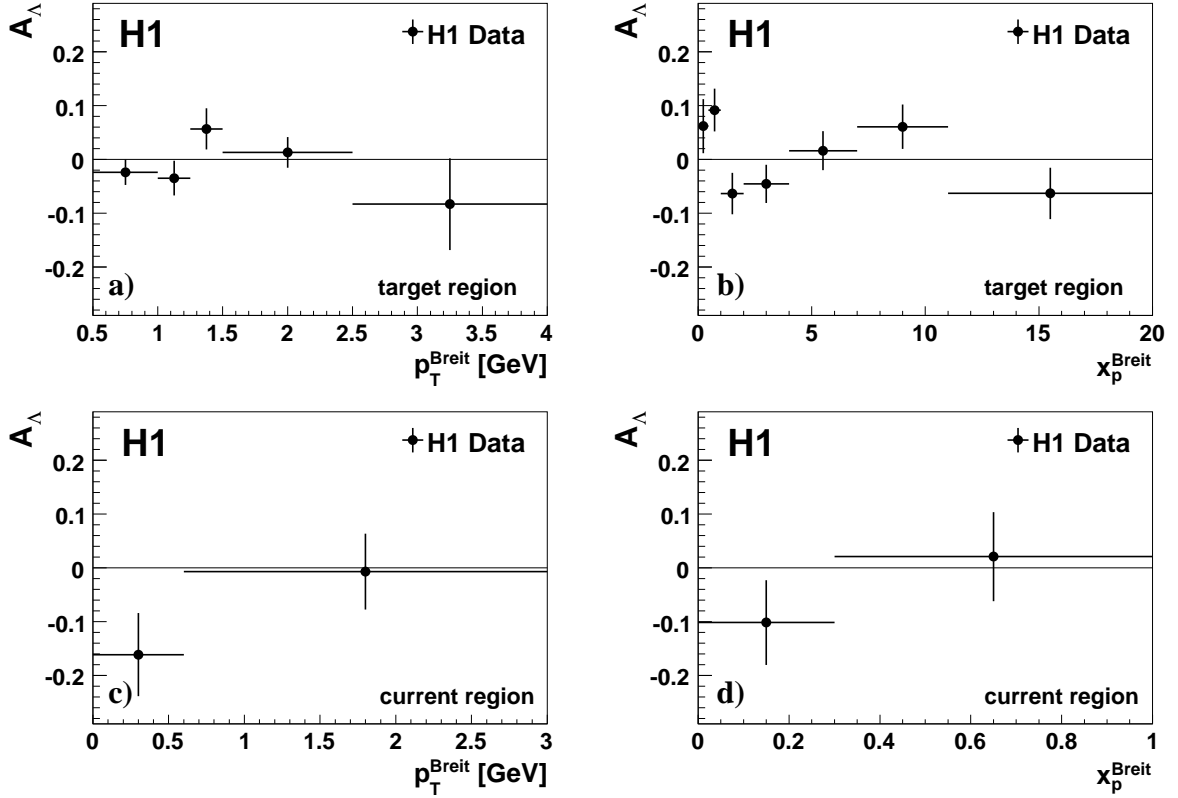
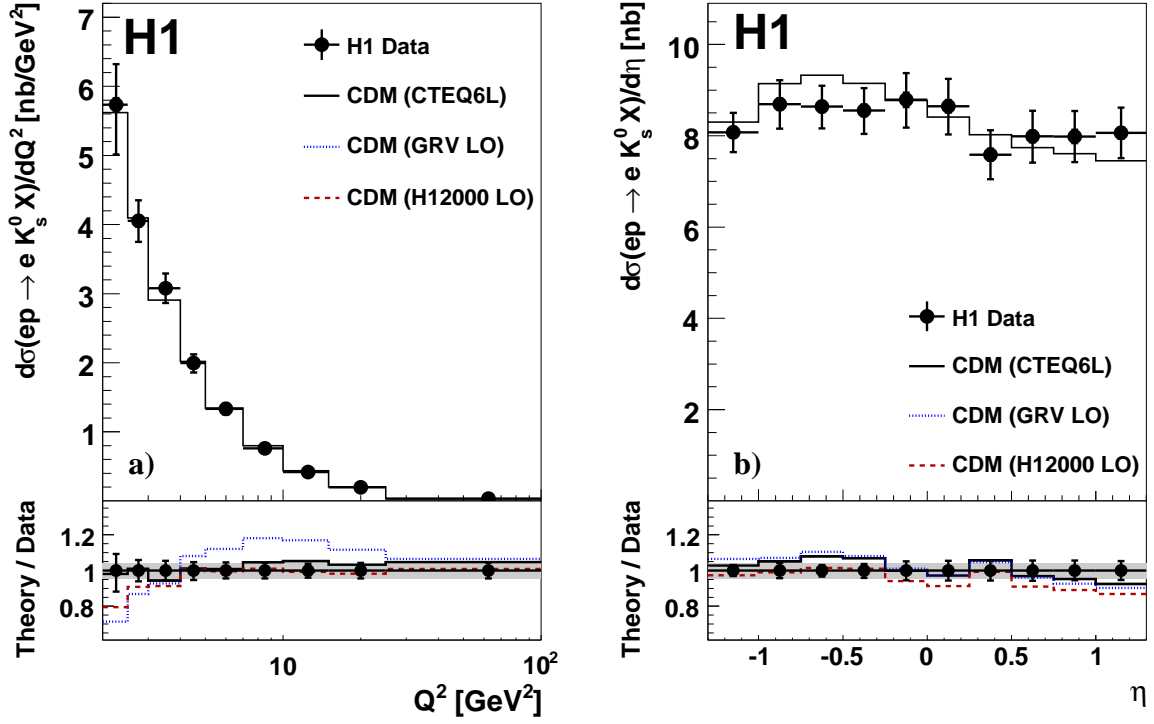


Figure 9: The asymmetry A_Λ of the differential production cross sections of the Λ and $\bar{\Lambda}$ baryons measured in the Breit frame as a function of transverse momentum p_T^{Breit} and momentum fraction x_p^{Breit} in the target hemisphere (a, b) and in the current hemisphere (c, d). The asymmetry is defined as $A_\Lambda = [\sigma_{vis}(ep \rightarrow e\Lambda X) - \sigma_{vis}(ep \rightarrow e\bar{\Lambda} X)] / [\sigma_{vis}(ep \rightarrow e\Lambda X) + \sigma_{vis}(ep \rightarrow e\bar{\Lambda} X)]$. The error bars show the statistical uncertainty.

$$ep \rightarrow e K_s^0 X$$



$$ep \rightarrow e \Lambda X$$

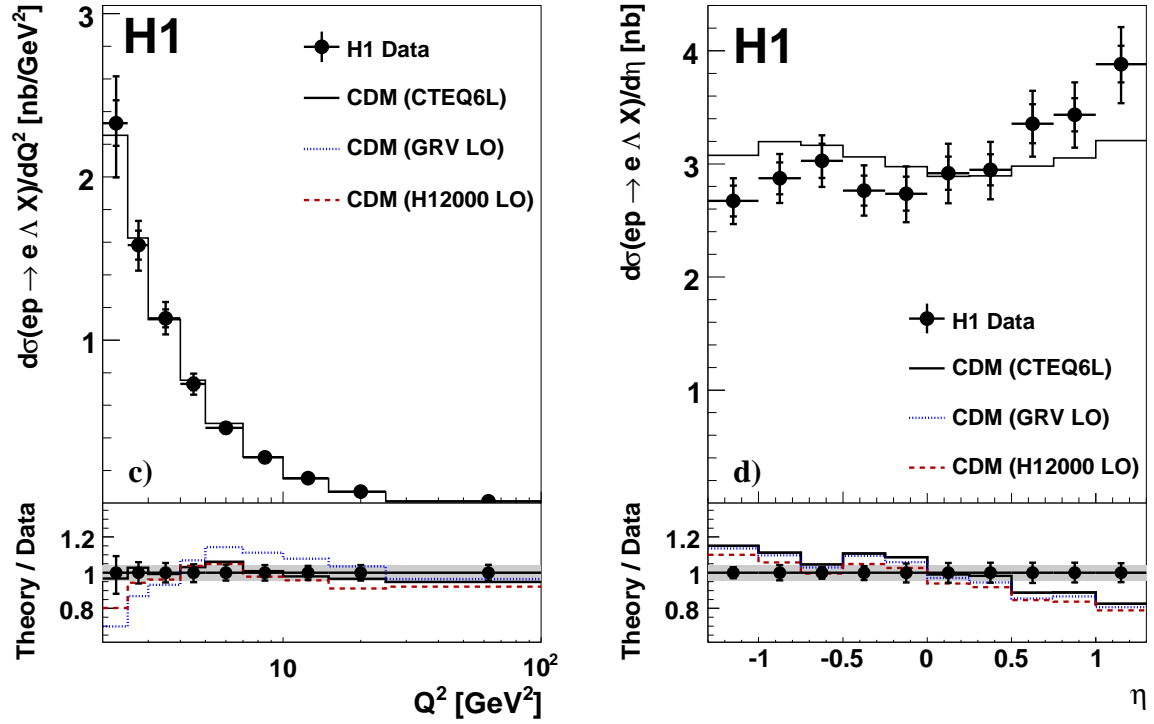


Figure 10: The differential production cross sections in the laboratory frame as a function of the event variable Q^2 and pseudorapidity η for the K_s^0 (a, b) and Λ (c, d). Overlaid are CDM predictions for $\lambda_s = 0.286$ using three different proton PDFs: CTEQ6L, GRV-94 (LO) and H1 2000 LO. More details in the caption of figure 4.

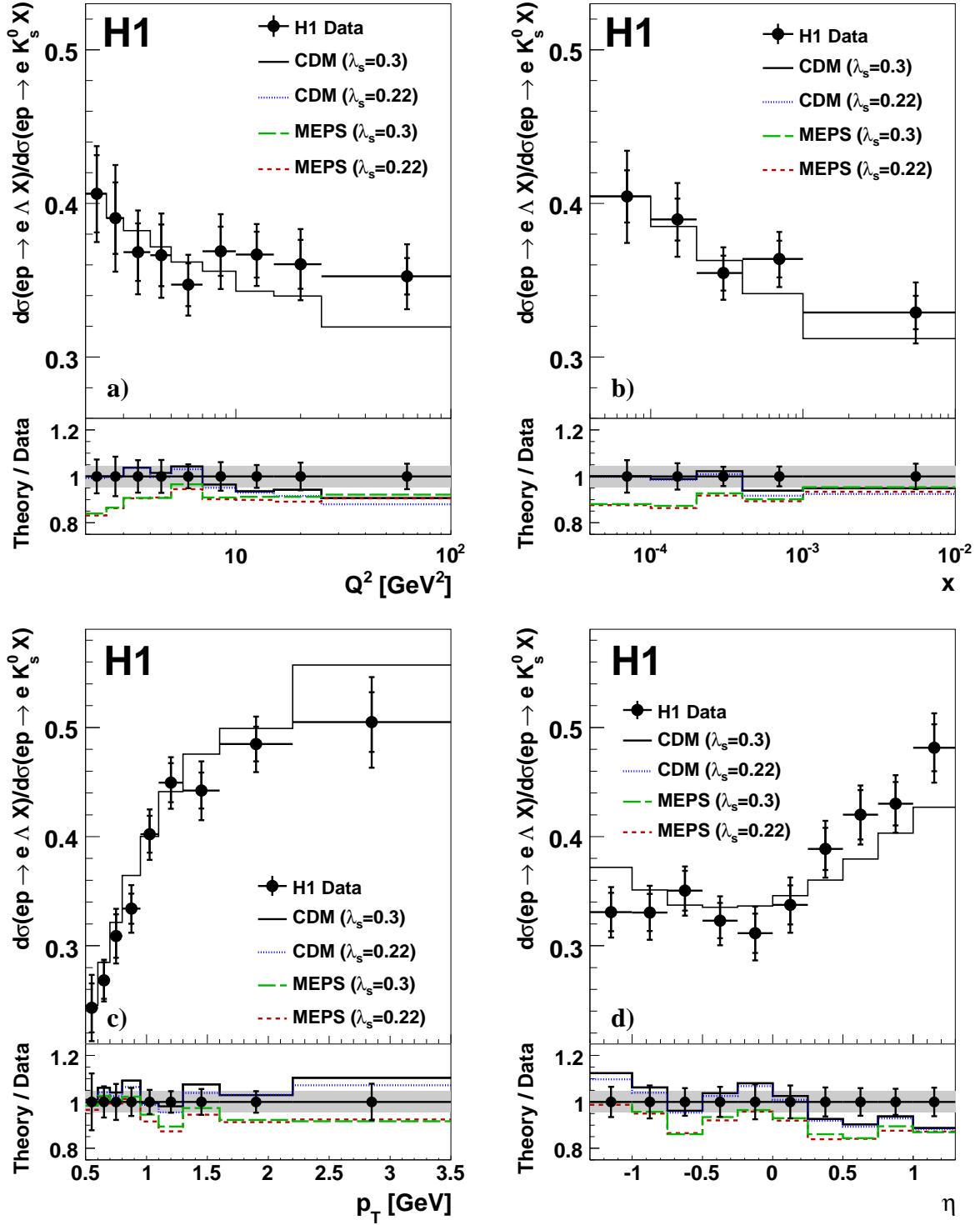
$$ep \rightarrow e \Lambda X / ep \rightarrow e K_s^0 X$$


Figure 11: The ratio of the differential production cross sections for Λ baryons and K_s^0 mesons in the laboratory frame as a function of the a) photon virtuality squared Q^2 , b) Bjorken scaling variable x , c) transverse momentum p_T and d) pseudorapidity η . More details in the caption of figure 4.

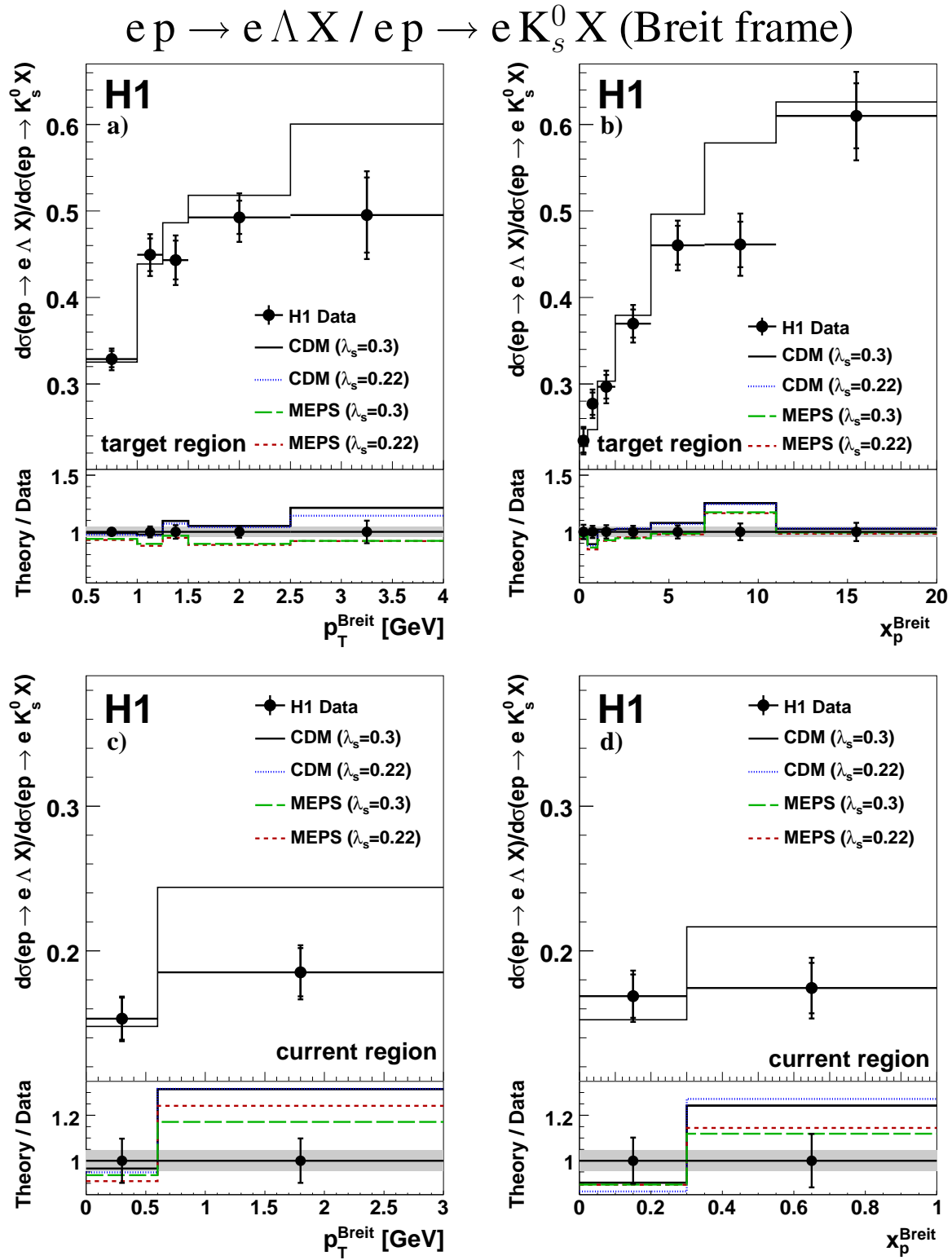


Figure 12: The ratio of the differential production cross sections for Λ baryons and K_s^0 mesons in the Breit frame as a function of transverse momentum p_T^{Breit} and momentum fraction x_p^{Breit} in the target hemisphere (a, b) and in the current hemisphere (c, d). More details in the caption of figure 4.

$$ep \rightarrow e K_s^0 X / ep \rightarrow e h^\pm X$$

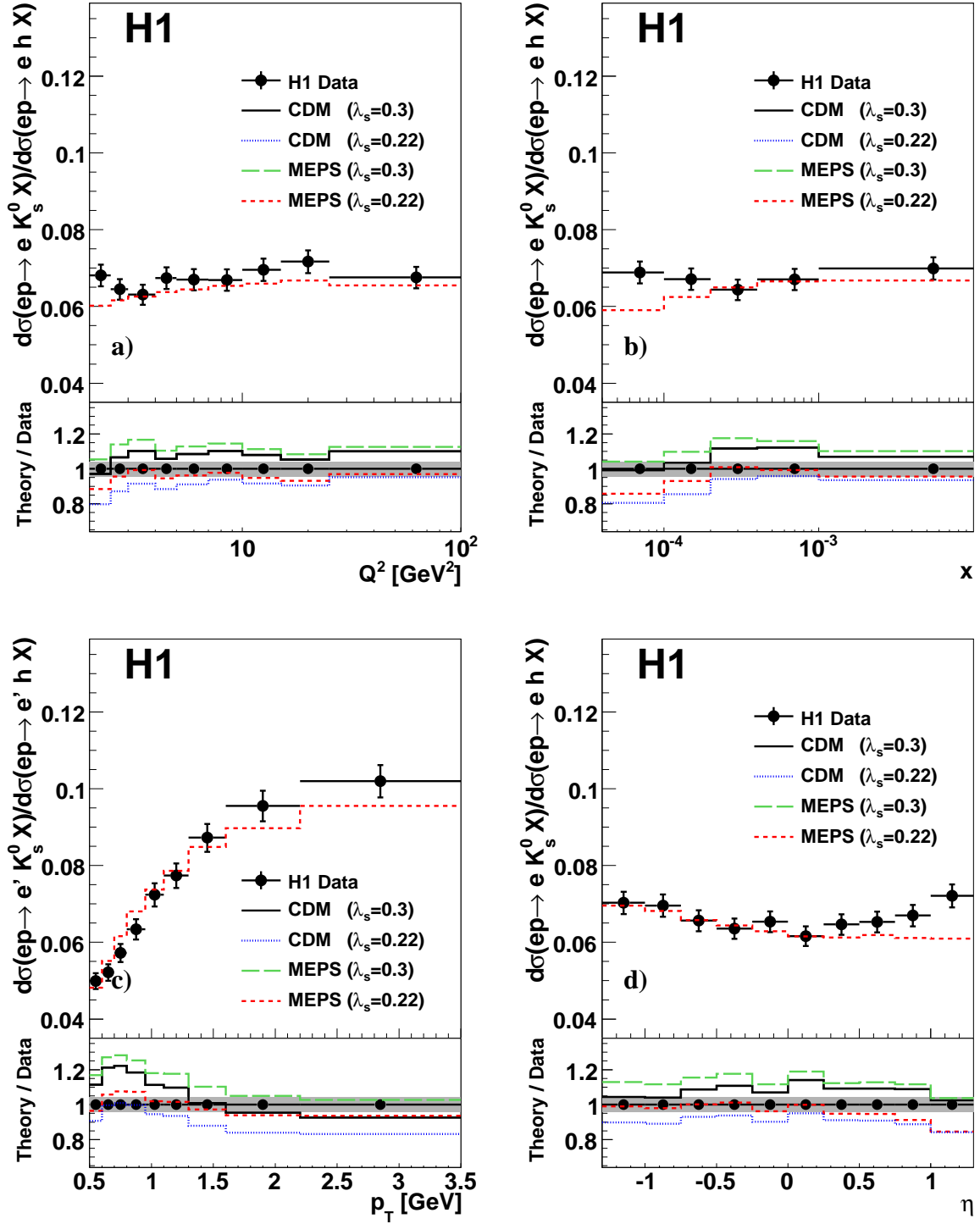


Figure 13: The ratio of the differential production cross sections for K_s^0 mesons and charged hadrons in the laboratory frame as a function of the a) photon virtuality squared Q^2 , b) Bjorken scaling variable x , c) transverse momentum p_T and d) pseudorapidity η . More details in the caption of figure 4.

$ep \rightarrow e K_s^0 X$				
Q^2 [GeV ²]	$d\sigma/dQ^2$	stat.	syst. (+)	syst. (-)
	[nb/GeV ²]			
2 – 2.5	5.73	0.10	0.58	0.71
2.5 – 3	4.05	0.08	0.29	0.29
3 – 4	3.08	0.05	0.21	0.21
4 – 5	2.00	0.03	0.12	0.13
5 – 7	1.332	0.018	0.082	0.082
7 – 10	0.764	0.011	0.045	0.047
10 – 15	0.417	0.006	0.023	0.024
15 – 25	0.197	0.003	0.012	0.012
25 – 100	0.0340	0.0004	0.0020	0.0021
x	$d\sigma/dx$	stat.	syst. (+)	syst. (-)
	[μ b]			
0.00004 – 0.0001	69.4	1.0	4.4	4.4
0.0001 – 0.0002	51.7	0.6	3.2	3.3
0.0002 – 0.0004	24.0	0.3	1.4	1.5
0.0004 – 0.001	7.07	0.07	0.43	0.43
0.001 – 0.01	0.315	0.004	0.019	0.019
p_T [GeV]	$d\sigma/dp_T$	stat.	syst. (+)	syst. (-)
	[nb/GeV]			
0.5 – 0.6	34.6	0.5	2.0	2.1
0.6 – 0.7	29.6	0.4	1.7	1.7
0.7 – 0.8	25.5	0.4	1.4	1.5
0.8 – 0.9	20.4	0.3	1.1	1.2
0.9 – 1.1	15.2	0.2	0.9	0.9
1.1 – 1.3	10.46	0.14	0.61	0.63
1.3 – 1.6	6.91	0.10	0.46	0.46
1.6 – 2.2	3.13	0.04	0.20	0.20
2.2 – 3.5	0.83	0.02	0.06	0.06
η	$d\sigma/d\eta$	stat.	syst. (+)	syst. (-)
	[nb]			
-1.3 – -1	8.08	0.12	0.41	0.42
-1 – -0.75	8.69	0.13	0.51	0.52
-0.75 – -0.5	8.64	0.12	0.44	0.46
-0.5 – -0.25	8.56	0.13	0.47	0.50
-0.25 – 0	8.79	0.16	0.56	0.59
0 – 0.25	8.65	0.14	0.58	0.60
0.25 – 0.5	7.58	0.13	0.52	0.52
0.5 – 0.75	7.99	0.13	0.55	0.56
0.75 – 1	7.98	0.15	0.54	0.54
1 – 1.3	8.06	0.13	0.54	0.54

Table 2: The differential K_s^0 cross-section values as a function of Q^2 , x , p_T and η in the visible region defined by $2 < Q^2 < 100$ GeV² and $0.1 < y < 0.6$. The bin ranges, the bin averaged cross section values, the statistical and the positive and negative systematic uncertainties are listed.

$ep \rightarrow e \Lambda X$				
Q^2 [GeV ²]	$d\sigma/dQ^2$	stat.	syst. (+)	syst. (-)
	[nb/GeV ²]			
2 - 2.5	2.33	0.14	0.25	0.30
2.5 - 3	1.58	0.09	0.12	0.13
3 - 4	1.13	0.05	0.08	0.08
4 - 5	0.73	0.04	0.05	0.05
5 - 7	0.462	0.018	0.028	0.030
7 - 10	0.282	0.012	0.019	0.020
10 - 15	0.153	0.006	0.009	0.009
15 - 25	0.071	0.003	0.004	0.004
25 - 100	0.0120	0.0004	0.0006	0.0006
x	$d\sigma/dx$	stat.	syst. (+)	syst. (-)
	[μ b]			
0.00004 - 0.0001	28.1	1.1	2.0	2.0
0.0001 - 0.0002	20.1	0.7	1.4	1.4
0.0002 - 0.0004	8.5	0.3	0.5	0.5
0.0004 - 0.001	2.57	0.08	0.15	0.15
0.001 - 0.01	0.104	0.003	0.006	0.006
p_T [GeV]	$d\sigma/dp_T$	stat.	syst. (+)	syst. (-)
	[nb/GeV]			
0.5 - 0.6	8.4	0.8	0.8	0.8
0.6 - 0.7	8.0	0.5	0.4	0.5
0.7 - 0.8	7.9	0.5	0.5	0.5
0.8 - 0.9	6.8	0.3	0.5	0.5
0.9 - 1.1	6.1	0.2	0.4	0.4
1.1 - 1.3	4.70	0.18	0.29	0.30
1.3 - 1.6	3.05	0.10	0.20	0.20
1.6 - 2.2	1.52	0.05	0.09	0.09
2.2 - 3.5	0.42	0.02	0.02	0.02
η	$d\sigma/d\eta$	stat.	syst. (+)	syst. (-)
	[nb]			
-1.3 - -1	2.67	0.14	0.15	0.15
-1 - -0.75	2.87	0.14	0.16	0.17
-0.75 - -0.5	3.03	0.15	0.17	0.17
-0.5 - -0.25	2.76	0.13	0.18	0.18
-0.25 - 0	2.74	0.15	0.19	0.20
0 - 0.25	2.92	0.15	0.21	0.22
0.25 - 0.5	2.95	0.14	0.21	0.22
0.5 - 0.75	3.36	0.17	0.23	0.23
0.75 - 1	3.43	0.15	0.25	0.25
1 - 1.3	3.88	0.16	0.28	0.31

Table 3: The differential Λ cross-section values as a function of Q^2 , x , p_T and η . More details in caption of table 2.

$ep \rightarrow e K_s^0 X$				
p_T^{Breit} target [GeV]	$d\sigma/dp_T^{Breit}$	stat.	syst. (+)	syst. (-)
		[nb/GeV]		
0.5 – 1	21.20	0.19	1.20	1.23
1 – 1.25	10.05	0.16	0.57	0.57
1.25 – 1.5	6.12	0.13	0.35	0.37
1.5 – 2.5	2.04	0.04	0.12	0.12
2.5 – 4	0.230	0.008	0.011	0.011
p_T^{Breit} current [GeV]	$d\sigma/dp_T^{Breit}$	stat.	syst. (+)	syst. (-)
		[nb/GeV]		
0 – 0.6	2.00	0.05	0.14	0.16
0.6 – 3	0.277	0.009	0.031	0.036
x_p^{Breit} target	$d\sigma/dx_p^{Breit}$	stat.	syst. (+)	syst. (-)
		[nb]		
0 – 0.45	4.01	0.08	0.22	0.23
0.45 – 1	5.43	0.09	0.39	0.42
1 – 2	3.66	0.05	0.25	0.25
2 – 4	2.03	0.03	0.11	0.11
4 – 7	0.984	0.016	0.05	0.05
7 – 11	0.478	0.011	0.026	0.028
11 – 20	0.167	0.005	0.011	0.013
x_p^{Breit} current	$d\sigma/dx_p^{Breit}$	stat.	syst. (+)	syst. (-)
		[nb]		
0 – 0.3	3.27	0.08	0.18	0.20
0.3 – 1	1.20	0.04	0.14	0.17

Table 4: The differential K_s^0 cross-section values as a function of p_T^{Breit} and x_p^{Breit} in the target and current hemispheres of the Breit frame. More details in caption of table 2.

$ep \rightarrow e \Lambda X$				
p_T^{Breit} target [GeV]	$d\sigma/dp_T^{Breit}$	stat.	syst. (+)	syst. (-)
		[nb/GeV]		
0.5 – 1	6.97	0.19	0.38	0.40
1 – 1.25	4.52	0.17	0.28	0.28
1.25 – 1.5	2.71	0.13	0.17	0.17
1.5 – 2.5	1.01	0.04	0.06	0.06
2.5 – 4	0.114	0.009	0.007	0.008
p_T^{Breit} current [GeV]	$d\sigma/dp_T^{Breit}$	stat.	syst. (+)	syst. (-)
		[nb/GeV]		
0 – 0.6	0.307	0.028	0.017	0.018
0.6 – 3	0.051	0.004	0.004	0.004
x_p^{Breit} target	$d\sigma/dx_p^{Breit}$	stat.	syst. (+)	syst. (-)
		[nb]		
0 – 0.45	0.94	0.05	0.05	0.06
0.45 – 1	1.51	0.07	0.11	0.12
1 – 2	1.09	0.05	0.08	0.09
2 – 4	0.75	0.03	0.05	0.05
4 – 7	0.45	0.02	0.03	0.03
7 – 11	0.220	0.011	0.015	0.016
11 – 20	0.102	0.006	0.008	0.008
x_p^{Breit} current	$d\sigma/dx_p^{Breit}$	stat.	syst. (+)	syst. (-)
		[nb]		
0 – 0.3	0.55	0.05	0.04	0.04
0.3 – 1	0.21	0.02	0.03	0.03

Table 5: The differential Λ cross-section values as a function of p_T^{Breit} and x_p^{Breit} in the target and current hemispheres of the Breit frame. More details in caption of table 2.

$R(\Lambda/K_s^0)$				
Q^2 [GeV ²]	$R(\Lambda/K_s^0)$	stat.	syst. (+)	syst. (-)
2 – 2.5	0.406	0.025	0.018	0.019
2.5 – 3	0.390	0.020	0.030	0.030
3 – 4	0.368	0.019	0.020	0.020
4 – 5	0.366	0.020	0.018	0.019
5 – 7	0.347	0.014	0.014	0.014
7 – 10	0.369	0.016	0.018	0.019
10 – 15	0.367	0.015	0.013	0.014
15 – 25	0.360	0.016	0.017	0.017
25 – 100	0.353	0.012	0.017	0.018
x	$R(\Lambda/K_s^0)$	stat.	syst. (+)	syst. (-)
0.00004 – 0.0001	0.405	0.017	0.024	0.025
0.0001 – 0.0002	0.390	0.014	0.019	0.020
0.0002 – 0.0004	0.355	0.011	0.012	0.013
0.0004 – 0.001	0.364	0.012	0.013	0.014
0.001 – 0.01	0.329	0.011	0.016	0.017
p_T [GeV]	$R(\Lambda/K_s^0)$	stat.	syst. (+)	syst. (-)
0.5 – 0.6	0.24	0.02	0.02	0.02
0.6 – 0.7	0.268	0.017	0.009	0.010
0.7 – 0.8	0.309	0.020	0.015	0.016
0.8 – 0.9	0.334	0.014	0.016	0.017
0.9 – 1.1	0.402	0.017	0.015	0.016
1.1 – 1.3	0.450	0.018	0.015	0.016
1.3 – 1.6	0.442	0.016	0.021	0.022
1.6 – 2.2	0.485	0.016	0.019	0.020
2.2 – 3.5	0.505	0.027	0.031	0.032
η	$R(\Lambda/K_s^0)$	stat.	syst. (+)	syst. (-)
-1.3 – -1	0.331	0.018	0.015	0.015
-1 – -0.75	0.330	0.017	0.018	0.018
-0.75 – -0.5	0.350	0.018	0.013	0.014
-0.5 – -0.25	0.323	0.016	0.015	0.016
-0.25 – 0	0.311	0.018	0.017	0.017
0 – 0.25	0.337	0.018	0.018	0.018
0.25 – 0.5	0.389	0.019	0.017	0.018
0.5 – 0.75	0.420	0.023	0.014	0.015
0.75 – 1	0.430	0.020	0.017	0.018
1 – 1.3	0.48	0.02	0.02	0.02

Table 6: The values of the ratio $R(\Lambda/K_s^0)$ of the differential cross-sections for Λ baryons and K_s^0 mesons as a function of Q^2 , x , p_T and η . More details in caption of table 2.

$R(\Lambda/K_s^0)$				
p_T^{Breit} target [GeV]	$R(\Lambda/K_s^0)$	stat.	syst. (+)	syst. (-)
0.5 – 1	0.329	0.009	0.008	0.009
1 – 1.25	0.449	0.019	0.015	0.016
1.25 – 1.5	0.443	0.023	0.017	0.018
1.5 – 2.5	0.493	0.019	0.020	0.021
2.5 – 4	0.495	0.043	0.026	0.027
p_T^{Breit} current [GeV]	$R(\Lambda/K_s^0)$	stat.	syst. (+)	syst. (-)
0 – 0.6	0.153	0.015	0.005	0.005
0.6 – 3	0.185	0.017	0.008	0.008
x_p^{Breit} target	$R(\Lambda/K_s^0)$	stat.	syst. (+)	syst. (-)
0 – 0.45	0.235	0.014	0.008	0.008
0.45 – 1	0.277	0.013	0.010	0.011
1 – 2	0.297	0.014	0.013	0.013
2 – 4	0.370	0.016	0.014	0.015
4 – 7	0.460	0.022	0.017	0.018
7 – 11	0.46	0.03	0.02	0.03
11 – 20	0.61	0.04	0.03	0.04
x_p^{Breit} current	$R(\Lambda/K_s^0)$	stat.	syst. (+)	syst. (-)
0 – 0.3	0.169	0.015	0.009	0.009
0.3 – 1	0.174	0.017	0.012	0.012

Table 7: The values of the ratio $R(\Lambda/K_s^0)$ of the differential cross-sections for Λ baryons and K_s^0 mesons as a function of p_T^{Breit} and x_p^{Breit} in the target and current hemispheres of the Breit frame. More details in caption of table 2.

$R(K_s^0/h^\pm)$				
Q^2 [GeV ²]	$R(K_s^0/h^\pm)$	stat.	syst. (+)	syst. (-)
2.0 – 2.5	0.0681	0.0002	0.0028	0.0029
2.5 – 3.0	0.0645	0.0001	0.0026	0.0027
3.0 – 4.0	0.0631	0.0002	0.0026	0.0027
4.0 – 5.0	0.0674	0.0002	0.0028	0.0028
5.0 – 7.0	0.0670	0.0002	0.0027	0.0028
7.0 – 10.0	0.0669	0.0002	0.0027	0.0028
10.0 – 15.0	0.0696	0.0002	0.0029	0.0029
15.0 – 25.0	0.0717	0.0002	0.0029	0.0030
25.0 – 100.0	0.0676	0.0002	0.0028	0.0028
x	$R(K_s^0/h^\pm)$	stat.	syst. (+)	syst. (-)
0.00004 – 0.0001	0.0689	0.0002	0.0028	0.0029
0.0001 – 0.0002	0.0671	0.0002	0.0027	0.0028
0.0002 – 0.0004	0.0644	0.0001	0.0026	0.0027
0.0004 – 0.001	0.0671	0.0002	0.0027	0.0028
0.001 – 0.01	0.0699	0.0002	0.0028	0.0029
p_T [GeV]	$R(K_s^0/h^\pm)$	stat.	syst. (+)	syst. (-)
0.5 – 0.6	0.0499	0.0001	0.0020	0.0021
0.6 – 0.7	0.0522	0.0002	0.0021	0.0022
0.7 – 0.8	0.0572	0.0002	0.0023	0.0024
0.8 – 0.9	0.0633	0.0002	0.0026	0.0027
0.9 – 1.1	0.0723	0.0002	0.0030	0.0030
1.1 – 1.3	0.0773	0.0002	0.0032	0.0032
1.3 – 1.6	0.0872	0.0003	0.0036	0.0037
1.6 – 2.2	0.0955	0.0003	0.0039	0.0040
2.2 – 3.5	0.1020	0.0003	0.0042	0.0043
η	$R(K_s^0/h^\pm)$	stat.	syst. (+)	syst. (-)
-1.3 – -1	0.0700	0.0002	0.0029	0.0030
-1 – -0.75	0.0696	0.0002	0.0029	0.0029
-0.75 – -0.5	0.0656	0.0002	0.0027	0.0028
-0.5 – -0.25	0.0635	0.0002	0.0026	0.0027
-0.25 – 0	0.0654	0.0002	0.0027	0.0027
0 – 0.25	0.0616	0.0002	0.0025	0.0026
0.25 – 0.5	0.0646	0.0002	0.0027	0.0027
0.5 – 0.75	0.0653	0.0002	0.0027	0.0027
0.75 – 1	0.0670	0.0002	0.0027	0.0028
1 – 1.3	0.0721	0.0002	0.0030	0.0030

Table 8: The values of the ratio of the differential production cross sections for K_s^0 mesons and charged hadrons as a function of Q^2 , x , p_T and η . More details in caption of table 2.